Politecnico di Torino

DEPARTMENT OF MECHANICAL AND AEROSPACE ENGINEERING

Master degree course in Aerospace Engineering

Master Degree Thesis

Bio inspired smart materials applied to Spacecraft Thermal Control

Candidate
Luca Casonato

Thesis advisors
Prof. Emma Angelini
Prof. Sabrina Grassini

Internship tutor
Eng. Federica Tessarin
(Thales Alenia Space Italy)

Research supervisor
Ph.D. Eng. Tiziano Schillaci
(Thales Alenia Space Italy)

2017-2018

Summary

The present thesis investigates the performance of an innovative radiator for space applications which incorporates surfaces with programmed thermal emissivity behaviour. This is achieved through the development of bioinspired anisotropic materials with a predetermined attitude to transform their shape via microstructural rearrangements under temperature stimuli. The self-shape structure reacts in accordance to temperature of the surrounding environment or the incident radiative heat fluxes. The transformation of the structure reveals materials with different thermo optical properties, thus creating a surface with programmable and variable effective thermal emissivity.

A preliminary definition and optimization of the radiator design drivers was performed. Two optimization criteria were employed: 1) minimization of the high emissivity area of the radiator in Cold Case; 2) maximization of the global view factor of the radiator towards space in Hot Case mode. The dimensions of the responsive structures (fins) were the design variables. In this context, a parametric algorithm was used as the optimization tool. The new design was then modelled in ESATAN TMS workbench in order to carry out the thermal analysis for an overall simply satellite. A user-defined subroutine interfacing ESATAN TMS was developed in order to create temperature dependent tables of environmental loads to simulate the temperature-varying surface geometry.

In conclusion the performance of this innovative radiator was compared to a conventional design, for the same operational conditions. The use of such adaptable structures ensures to the spacecraft thermal control system to rely on a less complex, heavy, expensive and more reliable passive solution. So programmable thermal emissivity structures based on bioinspired self-shape materials show better features than mechanical devices such as louvres as well as microelectromechanical systems (MEMs), which incorporate hinges and actuation mechanisms, and therefore the firsts are preferred to the latter.

Sommario

La presente tesi è rivolta allo studio delle prestazioni di un innovativo radiatore per applicazioni spaziali, il quale incorpora superfici in grado di variare la propria emissività in modo programmato. Questo singolare comportamento viene realizzato attraverso lo sviluppo di materiali ad alta anisotropia capaci di rispondere agli stimoli dell'ambiente che li circonda. Si tratta di materiali che, ispirati ai movimenti complessi delle piante, modificano la propria esposizione all'ambiente esterno attraverso una ridistribuzione geometrica delle microstrutture che li compongono, al fine di modulare lo smaltimento di calore verso l'ambiente. I parametri esterni che stimolano la reazione di queste superfici sono la temperatura e il flusso di calore incidente per radiazione. La trasformazione delle microstrutture mobili consente di rivelare, alternativamente, materiali dalle diverse proprietà termo-ottiche, realizzando superfici in grado di variare la loro emissività effettiva in maniera programmata. Inizialmente è stata eseguita una definizione e una ottimizzazione preliminare delle variabili di progetto del radiatore. Sono stati seguiti due criteri di ottimizzazione: 1) minimizzare la superficie del radiatore ad alta emissività nel peggior caso freddo; 2) masssimizzare il fattore di vista globale del radiatore nel peggior caso caldo. Le dimensioni delle strutture mobili (alette) hanno rappresentato le variabili di ottimizzazione. Il *design*, così definito, è stato in seguito modellizzato in ESATAN TMS al fine di poter svolgere un'accurata analisi termica di un satellite semplificato, equipaggiato con l'innovativo radiatore. Per poter simulare delle superfici aventi geometria variabile con la temperatura, è stato realizzato un programma di calcolo dedicato alla creazione di tabelle contenenti i valori dei flussi ambientali dipendenti dalla temperatura. In fine, le prestazioni di questo innovativo radiatore sono state confrontate con quelle di un radiatore convenzionale, impiegato nelle medesime condizioni di lavoro. L'utilizzo di strutture adattabili, come quella qui proposta, consentono di realizzare dei sistemi di controllo termico basati su dispositivi passivi meno complessi, più leggeri, meno costosi e più affidabili. Pertanto, sistemi ad emissività variabile, costruiti con materiali a geometria variabile "bioispirati", presentano delle caratteristiche migliori rispetto ai comuni dispositivi meccanici, quali louvers e sistemi microelettromeccanici (MEMs), che incorporano cerniere e attuatori meccanici. Materiali ispirati alla Natura e in grado di auto adattarsi all'ambiente che li circonda, costituiscono una nuova promettente via alla progettazione di sistemi di gestione termica più efficienti in settori, come quello spaziale, dove la massa e l'affidabilità sono i requisiti dominanti.

Contents

List of Tables

List of Figures

Chapter 1

Introduction

Satellite equipment needs to be maintained within specific temperature ranges in order to ensure the best performance during its operational life and its survivability even in non-operational mode. This is achieved by using satellite radiators. The most dissipating equipment is typically linked to the radiators in two ways: by putting the equipment in direct contact with the panels radiators or by vehiculating the heat inside phase-change devices, typically heat-pipes, from remote unit to the same panels.

On one hand high radiator emissivity is recommended in WHC conditions allowing the radiators to face with the highest heat loads, i.e. internal electrical dissipations and environmental fluxes. On the other hand the adoption of materials with low solar absorptivity ensures very compact radiators. OSR perfectly fulfils these two requirements and therefore are frequently used in space applications. Figure 1.1 shows typical OSR finishes employed in space radiators.

Figure 1.1   Typical OSR for space application. Courtesy image of [20].

The radiator face exposed to space is completely covered with OSR tiles. The OSR has the peculiar property to radiate the IR radiation dissipated inside the spacecraft to deep space ($T_{env} = 3\,K$) thanks to high values of thermal emissivity ($\varepsilon > 0.80$) while rejecting at the same time a considerable amount of incoming solar energy due to a reflectivity $\rho = 0.80 \div 0.90$. Nevertheless during WCC phases, when the heat loads are the smallest, in particular during eclipse or interplanetary transfer journeys, the spacecraft equipment gets too cold due to constant high emissivity of the radiator that continues to reject to space the same heat flux as in the "hot" case. To overcome an excessive cooling heater dissipations are used to maintain the specified equipment temperature. As a consequence this has a direct influence on the battery storage capacity. To minimize the on-board power consumption, thus the battery size, ε and α of the radiator have to be as small as possible during eclipses whilst today technology provides constant and high values of emissivity ($\varepsilon > 0.8$) optimized in a WHC focused design.

A variable and programmable emissivity material reveals to be the best solution to reduce the energy loss from the radiators through the implementation of a high emissivity during hot phases and a low emissivity during cold cases, combined with a constant absorptivity during all phases. Promising approaches to variable effective thermal emissivity of surfaces are represented by:

- Thermochromic (TCH) and electrochromic (ECH) materials which passively, in the first case, or actively, in the second case, change their reflectance in the IR wavelength via an applied external stimulus (temperature or bias voltage);

- Vanadium dioxide (VO_2) anomalous thermal emittance profile strongly correlated with temperature;

- Adaptable structures with variable and programmable thermal radiative properties.

In order to make the new product competitive against the actual OSR devices the following design drivers have to be met [10]:

Table 1.1 Thermo-optical requirements for the new technological solution. [10]

Property	BOL	EOL
α	$\leq 0.06 \div 0.12$	≤ 0.2
ε	> 0.8	> 0.8

1.1   Biomimetic approach

In recent years, the use of technologies and materials based on the imitation of biological systems "Biomimetics" is becoming more and more predominant in engineering. The term "Biomimetics" can be defined as the practice of ideas and concepts of "reverse engineering" obtained from the observation of nature and its implementation in the field of technology. We seek not to replicate biological organisms *in toto*, but rather to abstract the biological principals by which organisms operate and survive. In nature plants and animals tend to adapt to their environment and are capable of very fast response to external stimuli thanks to an extremely high sensitivity. Moreover, in Nature complex movements are performed through very simple structures and usually multiple tasks are demanded to the same component. These properties would allow to drastically reduce the complexity of an engineering product, hence improving its reliability and integration within other systems. As a result, bioinspiration represent an enabling technology for the Aerospace industry, where compact and cost-effective solutions are the driving requirements.

We can identified two biomimetic approaches [22], which differ from each other at the starting point for development:

- bottom-up approach, in which biology pushes the process by starting with a question from biology (see Figure 1.2);

- top-down approach, in which technology pulls the process by starting with a question from engineering sciences (see Figure 1.3).

Let us see how the the two approaches differentiate from each other by considering the solution that will be studied in the present thesis and explaining the two possible flow processes that will lead to its development.

Figure 1.2 shows a simplified flow chart starting with the observation of plants natural behaviour which are capable of regulating their temperature by self-folding/self-shaping. The transferred principal is the alteration of the view factor and the material exposure towards the environment in order to manage the absorption/emission or reflection of thermal radiation. This is due to the multilayer anisotropic material properties of plants structure, which present different coefficients of thermal expansion (CTEs) leading to different degree of deformation of the structure according to the temperature level. The thermal concept behaviour is simulated with lumped-parameter method. The technical application consists of the implementation of radiators with adaptable skin for a typical space mission.
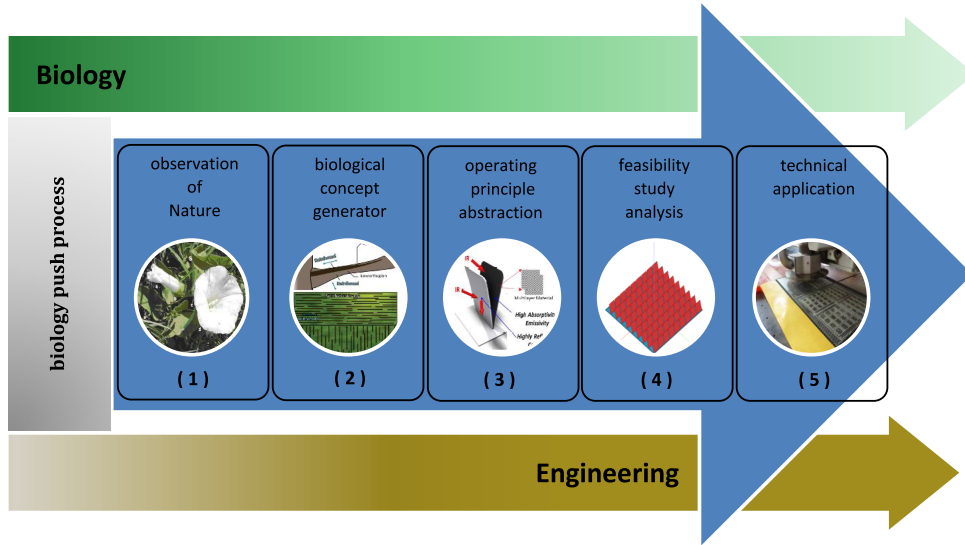
Figure 1.2   The bottom-up approach (biology push process) of the self-shaping radiator for thermal control of satellites.

Figure 1.3 illustrates the stepwise development of the bioinspired smart radiator in terms of a top-down approach (technology pull process). This represents the main development process adopted by Schillaci et al. [20].
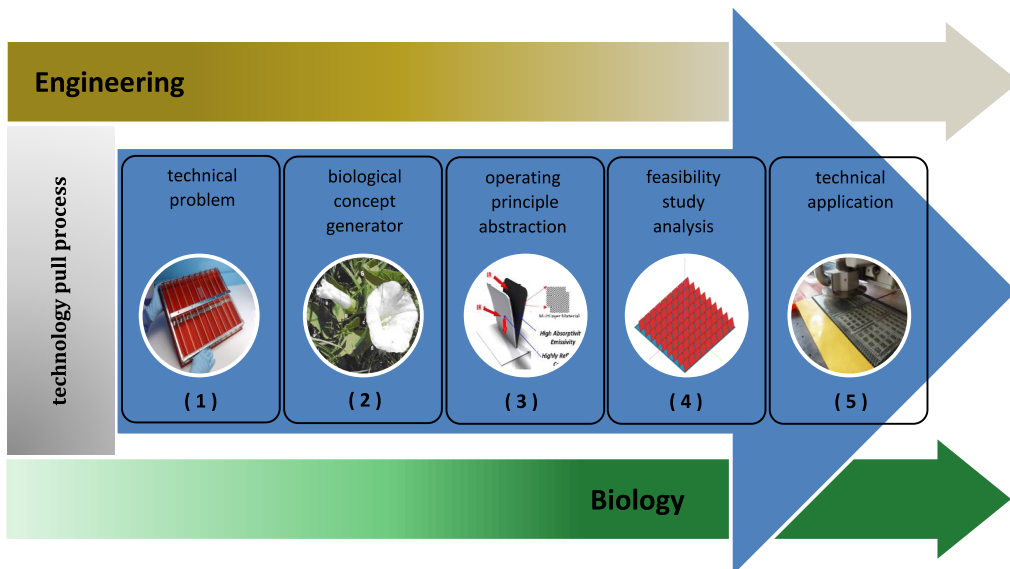
Figure 1.3   The top-down approach (technology pull process) of the self-shaping radiator for thermal control of satellites.

Variable emissivity/absorptivity structure have already been developed and studied, leading to the realization of complex, heavy mechanical devices such as louvres and micro-electromechanical systems (MEMs), which incorporate hinges and actuation mechanisms. The starting point of the development of the bioinspired smart radiator is the challenge to find materials and structures that are a priori tuned to passively react to external temperature stimuli. The biological concept generator is the thermonastic movements performed by plants, meaning "folding caused by a temperature stimulus" [1], in order to transform the shape of leaves/petals under a temperature stimulus. The operating principle is based on the large CTE mismatch between two fibrous anisotropic layers, that creates shape memory materials triggered by the development of internal stress induced by temperature stimuli. The thermal behaviour of the self-shape structure can be simulated with lumped parameter modelling as a smart radiator for a typical space mission. Technical applications consists of a surface made of a plethora of multi-layered fibrous anisotropic unit-cell structures.

1.2 Objectives

The Thermal Control Design Unit of the Competence Center Platform and Integration (CCPI-I) of Thales Alenia Space Italy (TASI) has started the development of a new generation of multifunctional materials with variable and programmable thermo-optical properties for a smart Space Mission Flying Thermal Control. The research project fits in the frame of Innovation Cluster R&D activities and aims at reducing the TCS allocations by providing a more efficient thermal system and passive thermal control. The solution proposed by [20] is drawn from Nature, where flowers' petals/leaves change their shape in order to handle the thermal energy exchange with the environment. The material under development is made of a plethora of unit-cell structures inspired to flowers natural behaviour, which are a priori tuned to passively respond to external temperature stimuli by changing their geometry and their material exposure thus either absorbing/emitting or reflecting thermal radiation accordingly. Therefore, the self-shaping capabilities via microstructural rearrangements of those adaptable arrays represent an innovative and smart way of providing thermal regulation for the spacecraft radiator.

The aim of the present thesis work is to demonstrate the effectiveness of the new spacecraft thermal control solution in terms of heater power saving and thermal gradients reduction compare to a classic radiator design for the same operational conditions. This is mainly achieved through a preliminary thermal design optimization study and the development of a user-defined subroutine for the creation of temperature dependent heat flux arrays in ESATAN-TMS.

1.3   Thesis structure

The thesis is divided in the following chapters:

Chapter 2   is a general introduction to the thermal control discipline, particularly in space applications. The first section deals with the description of the space thermal environment that a spacecraft has to face with during its entire mission. The second section concerns radiators with variable emissivity properties as one of the best solutions for providing high thermal control efficiency.

Chapter 3   is a survey of existing technologies, that allow variable thermo-optical properties, with a brief description of their basic mechanism of operation and their past and present application.

Chapter 4   focuses on the description of the bioinspired self-shape material and it is divided in three main sections. The first section explains the thermal concept design characterizing the responsive material, while the following section is dedicated to the theoretical explanation of the mechanism behind the actuation of the responsive structure. The potential materials to be adopted and their stacking sequence for the realization of the self-shape coating is also presented. The last section deals with the preliminary thermal design optimization of the smart self-shape array. Finally, the best trade-off solution is presented.

Chapter 5   concerns the thermal analysis of a simply small satellite equipped with the bioinspired self-shape coating for two type of space missions, namely a LEO and a MEO mission. On three of the four spacecraft's are mounted a radiator with implemented the optimized thermal design that was calculated in chapter 4. Results are then compared to those of a classical radiator configuration and discussed.

Chapter 6   summarizes the main conclusions in terms of advantages and disadvantages and the potential effectiveness coming from the application of the innovative coating to future spacecraft radiators and thermal management systems.

Chapter 2

Thermal control of Spacecraft

The aim of spacecraft thermal control is to manage the energy equilibrium between the overall system and the space environment where it operates in order to keep all the on-board systems within certain temperature ranges during their whole lifetime. For instance, a component of the equipment could, if encountering a temperature level which is too high, be damaged or its performance could be severely affected. Moreover, delicate electronics or optical components require a specified temperature stability in order to perform as efficiently as possible. Therefore, thermal requirements are usually given in terms of:

- **Operation temperature levels**, to ensure devices to perform optimally and to extend their lifetimes;

- **Survivable temperature levels**, to avoid critical temperature values that could irredeemably damage the equipment;

- **Thermal gradients**, to reduce temperatures variation in space and/or in time for certain payloads as a way to improve their sensitivity.

The satellite's payload and subsystems dictate all these thermal specifications. Typical temperature ranges for a satellite's components are described in Table 2.1. The level of temperature of a spacecraft is determined by the balance among the external environmental fluxes (e.g. solar, albedo, planet heat fluxes), the heat generated internally the spacecraft (e.g. by electronic equipment) and the heat rejected by the system to deep space. For the sake of the physical integrity of the satellite and for its efficient operation, it is important to calculate accurately all these sources of heat radiation and to select adequate thermal control materials.

In conclusion, the TCS seeks to maintain the overall temperature to an acceptable level and also to provide the most adequate temperature distribution within the spacecraft for all phases of the mission (e.g. launch, transfer orbit, operation in orbit).

Table 2.1   Typical operation thermal requirements for satellite's components.

Components	T_{min} (°C)	T_{max} (°C)	ΔT (°C)
Structures&Mechanisms:			
Carbon-based steels	-50	700	
Low carbon stainless steels	-273	700	
Lightweight alloys	-273	400	
Composite materials	-273	150	
Bearings	-45	65	
Electronic components	-10	40	
Batteries	-10	20	
Solar cells	-60	60	
Propulsion systems	propellant dependent		
Optical payload	15	20	$< 0.1 \div 0.5$
Sensors		-153	

In the following sections we will briefly recall the physical theory behind the design of a spacecraft thermal control subsystem. Specifically, we will focus our attention on the governing equations of heat transfer and the different mechanisms through which heat could be exchanged among two or more bodies in space. It follows a description of the thermal environment that the spacecraft will experience once in orbit, presenting the different heat sources that defined it. Finally, in a dedicated section, we will describe the main design approaches used to deal with space thermal issues.

2.1   Heat Transfer

Heat is that form of energy which occurs in the transfer from one body to another when they are at different temperature. The Second Law of Thermodynamics states the direction of the spontaneous heat transfer, i.e. from the hotter body to the colder one, whereas the First Law of Thermodynamics defines that the systems continue to exchange energy till they both reach a certain temperature value, namely the temperature of equilibrium. Hence, the First Law of Thermodynamics is a form of energy balance, which is described by the equation 2.1:

$$\frac{dU}{dt} = Q - W \tag{2.1}$$

The total internal energy (U) of a system is a property of the thermodynamic system, namely a sate function, and its variation is determined by the balance of work (W) and heat (Q), which indeed represent two quantities of transfer rather than state functions. For the thermal analysis of a spacecraft, the term (Q) represents the heat flux and (U) the energy generated by the internal equipment. Since the spacecraft does not perform any kind of work on the surrounding environment ($W = 0$), the equation 2.1 simplifies in:

$$\frac{dU}{dt} = Q = \mathrm{A}\,\mathrm{dx}\,\rho\,\mathrm{C}\,\frac{\mathrm{d}T}{\mathrm{d}t} \tag{2.2}$$

where (U), and thus (Q), is expressed via the product of the material's cross section (A), length (dx), density (ρ), specific heat capacity (C) and the temperature change in time ($\mathrm{d}T/\mathrm{d}t$) of the system.

The total net heat flux of the spacecraft is described by the difference between the heat flux entering the system (Q_{in}) and the heat flux leaving the system (Q_{out}):

$$Q_{\mathrm{net}} = Q_{\mathrm{in}} - Q_{\mathrm{out}} \tag{2.3}$$

Three ways of transfer can be distinguished:

- conduction

- convection

- radiation

It is possible that one of these three mechanisms of heat transfer prevails to the others. It is the case of space heat transfer, where the vacuum environment nullifies convective phenomenon, while conduction and, especially, radiation are the predominant ways of heat transfer.

2.1.1   Conduction

Conduction is that way of energy transfer within a material involving the exchange of kinetic energy of molecules at different energy level due to collisions between them. Since higher temperatures are associated with higher molecular energies, in the presence of a temperature gradient the energy transfer by conduction must then occur in the direction of decreasing temperature. The physical equation that regulates the rate of heat transfer by conduction for a one-dimensional plane wall (Figure 2.1) is expressed by the *Fourier's Law*:

$$q_{\mathrm{cond}} = \frac{k\,A}{L}\,(T_1 - T_2) \tag{2.4}$$

As it can be stated from equation (2.4) the wider is the contact area (A) and the temperature variation ($T_1 - T_2$), the more is the amount of energy transferred per unit time (q_{cond}).

Whereas, the heat transfer rate decreases as the path (L) becomes longer and longer, because heat has to pass through more material in the unit time. Moreover, the value of (q_{cond}) is directly affected by the thermal conductivity (k), that is a intrinsic property of the material.
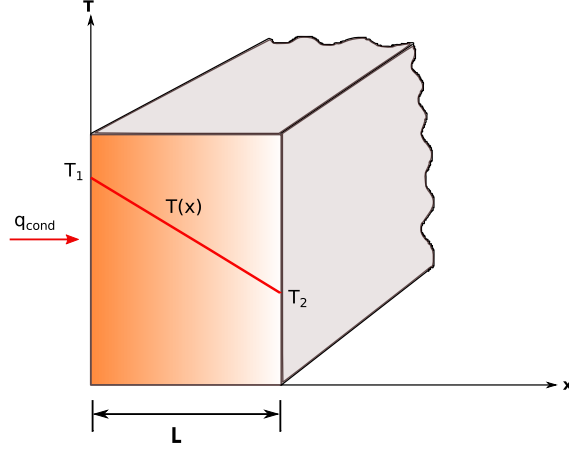
Figure 2.1   One-dimensional heat transfer by conduction.

In spacecraft applications, conduction plays a relevant role in the dissipation of heat produced by the onboard electronic equipment through the radiator panels. The variation of the temperature profile within the material can be assumed linear in most cases, thus leading to the definition of the linear conductor:

$$GL = \frac{k\,A}{L} \tag{2.5}$$

In conclusion, the (2.4) can be rewritten as:

$$q_{cond} = GL\,(T_1 - T_2) \tag{2.6}$$

2.1.2   Radiation

Any object with a temperature above the absolute zero emits energy in the form of electromagnetic radiation and it is also able to absorb that radiant energy. So, two bodies can exchange energy between each other by thermal radiation. This new way of heat transfer is governed by the amount of radiant energy emitted by an ideal black body, also known as Planck's Distribution Law:

$$E_{b\lambda}(\lambda,\,T) = \frac{2\pi\,C_1}{\lambda^5 \left(e^{\frac{C_2}{\lambda T}} - 1 \right)} \tag{2.7}$$

where (E_b) is the energy emitted/absorbed by the black body, (λ) is the wavelength, (T) is the absolute temperature of the black body, (C_1) and (C_2) are two constants defined as follows:

$$C_1 = 2\pi h c_0^2 = 3.7418 \times 10^{-16}\ W\ m^2$$
$$C_2 = hc_0/k = 14.388\ \mu m\ K$$

where the symbol (h) identifies the Planck's constant, 6.6261×10^{-34} J s, c_0 is the speed of light, 3×10^8 m/s, and k is the Boltzmann's constant, 1.3807×10^{-23} J/K.

Figure 2.2 illustrates Planck's Law as a function of wavelength and temperature. It is also reported the emissive power curve for a black body at temperature $T = 5777$ K, that is comparable to that of the Sun.
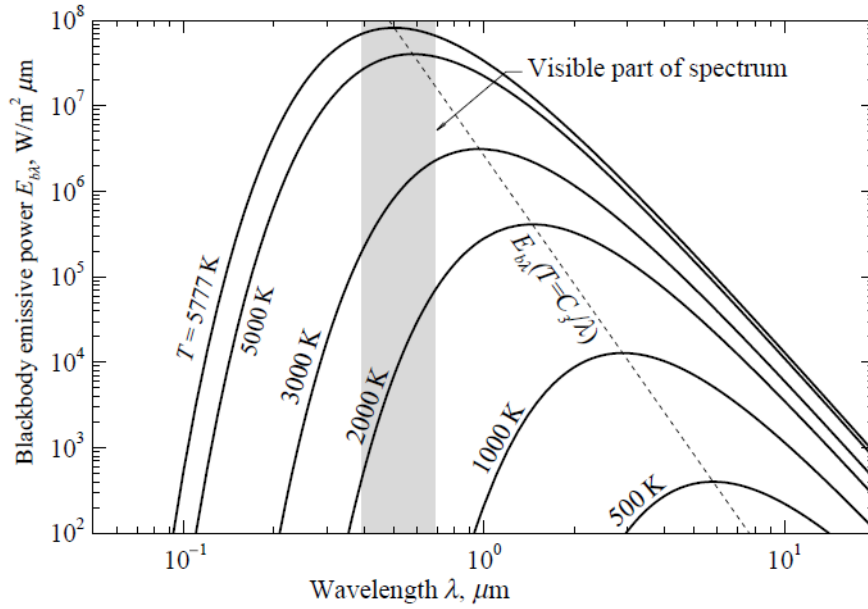
Figure 2.2   Black body emissive power spectrum.

Integrating equation (2.7) over all wavelengths, we obtain the total black body emissive power:

$$E_b(T) = \int_0^\infty E_b(\lambda,\ T)\ d\lambda = \sigma T^4 \qquad \left[W\,m^{-2}\right] \qquad (2.8)$$

where σ is the Stefan-Boltzmann constant, 5.669×10^{-8} W m^{-2} K^{-4}, and equation (2.8) is called Stefan-Boltzmann Law. This law underlines that the energy irradiated by a black body is proportional to the temperature to the fourth power. This is the reason why at very high temperature the heath transfer by radiation is predominant respect to the other forms of energy transfer.

11

2.1.3   Radiation properties of a real body

Equation (2.8) refers to a black body, which is an ideal object with the ability to absorb and emit all incident radiation. On the contrary, a real body cannot absorb all the incident radiation, but a fraction is reflected away from the medium and another fraction is transmitted through the material. Based on this considerations we define three fundamental radiative properties, also depicted in Figure 2.3 :

$$\textit{Reflectance,} \quad \rho = \frac{\text{reflected part of incoming radiation}}{\text{total incoming radiation}} \tag{2.9}$$

$$\textit{Absorptance,} \quad \alpha = \frac{\text{absorbed part of incoming radiation}}{\text{total incoming radiation}} \tag{2.10}$$

$$\textit{Transmittance,} \quad \tau = \frac{\text{transmitted part of incoming radiation}}{\text{total incoming radiation}} \tag{2.11}$$
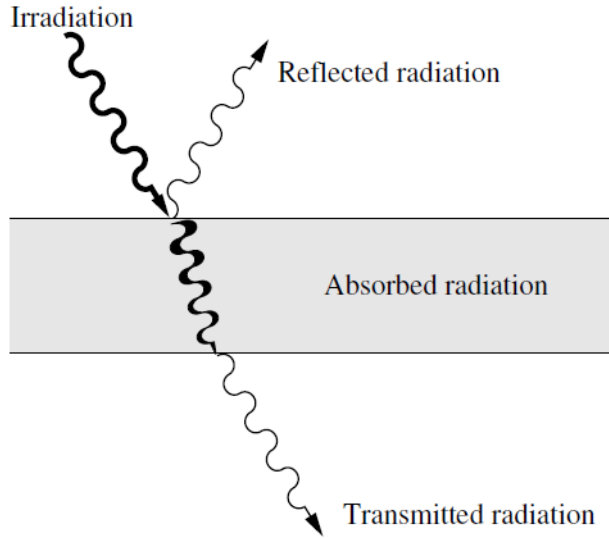
Figure 2.3   Radiation properties of a real body.

According to the energy conservation law, all radiation must be either reflected, absorbed, or transmitted, hence:

$$\rho + \alpha + \tau = 1 \tag{2.12}$$

In case of opaque bodies, $\tau = 0$ and:

$$\rho + \alpha = 1 \tag{2.13}$$

(2.9), (2.10), (2.11) are nondimensional values and may vary in magnitude between 0 and 1. Since, at a given temperature, the maximum possible energy emitted belongs to a black body, we can define a fourth nondimensional property:

$$\text{\textit{Emittance}}, \qquad \varepsilon = \frac{\text{energy emitted from a real body}}{\text{energy emitted by a black body at same temperature}} \qquad (2.14)$$

For real bodies we have $\varepsilon < 1$, while for ideal black bodies $\varepsilon = 1$.
At this point, we can calculated the total emissive energy of a real surface by multiplying equation (2.8) for the emissivity:

$$E = \varepsilon \sigma T^4 \qquad \left[\text{W m}^{-2}\right] \qquad (2.15)$$

When a surface reaches the thermal equilibrium, the emissivity equals the absorptivity:

$$\alpha = \varepsilon \qquad (2.16)$$

The (2.16) is known as Kirchhoff's Law and it requires the following two assumptions: the surface must be diffuse (i.e. surface properties are independent of direction) and grey (i.e. surface properties are independent of wavelength).

2.1.4   Radiative View Factors

The radiative view factor F_{ij} is defined as the fraction of the radiation leaving one surface that is intercepted by another [21].
We consider the radiative energy exchange between two finite areas, A_i and A_j, as shown in Figure 2.4. The view factors for the two infinitesimal areas, dA_i and dA_j, are:

$$F_{dA_i - dA_j} = \frac{\cos \theta_i \, \cos \theta_j}{\pi R^2} \, dA_i \, dA_j \qquad (2.17)$$

We denoted with θ the angle formed by the normal vector at the surface with the distance R. Integrating over the two areas, A_i and A_j, we can calculate the view factor between the two finite areas:

$$F_{A_i - A_j} = \frac{1}{A_i} \int_{A_i} \int_{A_j} \frac{\cos \theta_i \, \cos \theta_j}{\pi R^2} \, dA_i \, dA_j \qquad (2.18)$$

From an examination of the symmetry of this equation, we derived the Law of Reciprocity:

$$A_i \, F_{ij} = A_j \, F_{ji} \qquad (2.19)$$

As a direct consequence of the conservation requirement, from each of the N nodes inside a spacecraft, the sum of the view factors to surrounding equipment must be unity [21]:

$$\sum_{j=1}^{N} F_{ij} = 1 \qquad (2.20)$$

13
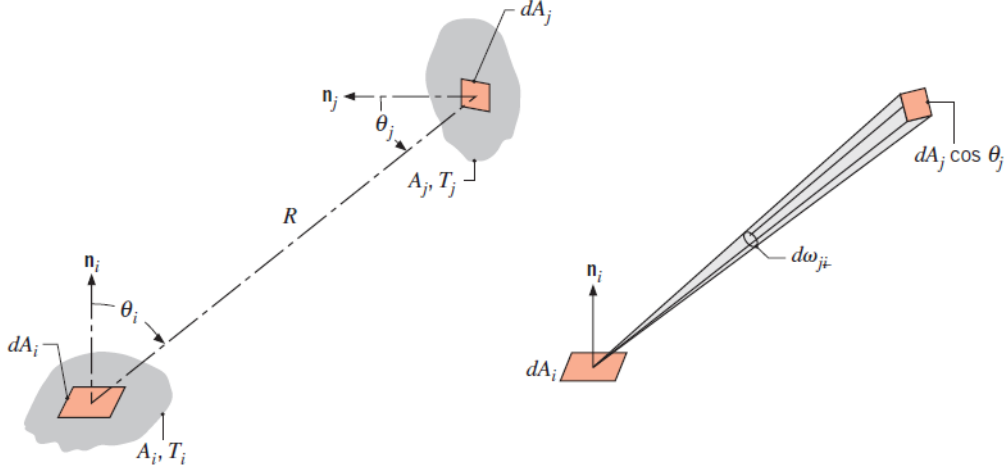
Figure 2.4   Radiative exchange between two finite surfaces A_i and A_j.

Since equation (2.18) becomes quite complicated to evaluate for complex geometries, many examples of standard configurations are available in the literature to make the task easier. For simple spacecraft designs, view factors can also be determined experimentally, for example by using a device known as factometer. For large and complex spacecraft configurations, sophisticated software tools have been developed in recent years, such as ESARAD, in order to overcome those limitations [21].

Summarizing the results obtained in the previous sections, we can conclude that radiative heat exchange between two surfaces is determined by three important parameters [21]:

- the surface temperatures (T_i, T_j)

- the radiative view factors (F_{ij})

- the surface properties (ε)

Therefore, considering diffuse surfaces, the amount of radiation leaving the surface i and absorbed by the surface j is:

$$Q_{ij} = A_i \, F_{ij} \, \varepsilon_{ij} \, (T_i^4 - T_j^4) \tag{2.21}$$

2.2 Space thermal environment

The principal sources of environmental heating on geocentric orbits are direct sunlight, incident sunlight reflected off the Earth (albedo), and the planetary (i.e. Earth) IR radiation. All these heat fluxes from space must be carefully balanced together with the energy dissipated by the spacecraft's internal electrical units against the IR radiation emitted by the spacecraft its self. For orbits over 150km the main process of heat exchange is represented by radiation.

2.2.1 Solar radiation source

Solar flux represent the most influential source of environmental heating for spacecraft in Earth orbit. Due to Earth's elliptical orbit, the sunlight striking our Planet is subjected to an approximately ±3.5% variation, depending on the distance of Earth from the Sun (see table 2.2). The average value of the intensity of sunlight at the mean Sun-Earth distance (1 AU), called solar constant, has been set by community's current agreement at the value of $1366.1\,W/m^2$. The currently measured 1-sigma variation of the composite dataset of space based measurements is approximately $0.6\,W/m^2$ with a long-term (yearly) smoothed solar cycle minimum to maximum relative variation about the mean value of $1.4\,W/m^2$ [9].

Table 2.2   Solar flux intensity values according to [9].

Solar constant at 1 AU	$1366.1\,W/m^2$
Solar energy flux at aphelion	$1321.6\,W/m^2$
Solar energy flux at perihelion	$1412.9\,W/m^2$

The values of solar flux at aphelion and at perihelion reported in table 1 are the results of the total integrated solar energy composed by nearly 7% ultraviolet (UV), 46% visible, and 47% near IR. It is clear from figure 2.5, that the visible light, in the range between 380 nm and 760 nm, is responsible of the greatest percentage of the total solar radiation.

The IR energy emitted by the Sun is of a much shorter wavelength compare to that emitted by a body near room-temperature (far IR) [7]. This represent a crucial point for thermal control in space, because it allows for the selection of thermal control finishes that are highly reflective in the solar spectrum but present high emissivity in the long-wavelength IR portion of the spectrum, as shown in figure 2.6. The heat flux generated by the Sun and absorbed by a spacecraft in geocentric orbit is defined as:

$$Q_{\text{Sun}} = \alpha\,J_{\text{S}}\,A\cos\theta \tag{2.22}$$

15
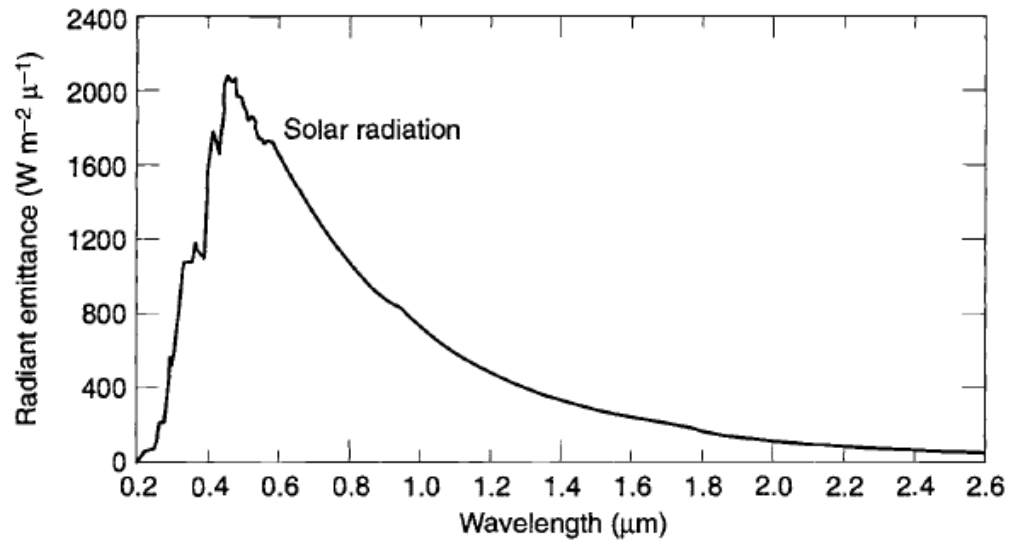
Figure 2.5 Solar spectral distribution.
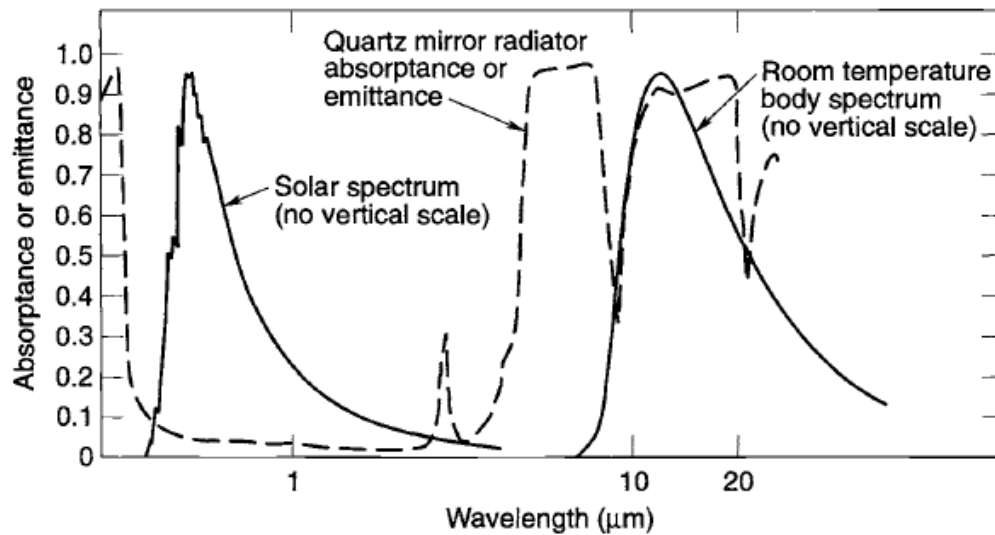
Figure 2.6 Solar spectral distribution.

16

where J_S is the solar constant according to table 2.2, α is the solar absorptance of the surface, A is the area of a flat surface, whose normal vector forms an angle θ with solar rays [21].

2.2.2 Albedo radiation source

A planet's albedo is usually expressed as the fraction of incident sunlight that is reflected back to space [7], and its value depends mainly on the sunlit portion of the Earth which the spacecraft can see [9]. Usually it is expressed as a percentage of incident sunlight with a diffusive behavior. Albedo is highly variable across the globe and depends on surface properties and cloud cover. It is also depends on the solar zenith angle [9]. For these reasons, averaged albedo values have to be used conscientiously, namely for short duration thermal analysis or for Sun-synchronous orbits where albedo is referred at specific local times [9]. Even if for the albedo is assumed an equal spectral shape as for sunlight, the actual albedo spectrum can change due to different surface's properties (materials have different susceptibility to absorption in certain wavelength bands, thus resulting in a highly variable spectrum) or to atmosphere [9]. The albedo factor is commonly expressed as a percentage of incident sunlight. Table 2.3 summarizes the average values of the albedo constant of the planets belonging to our solar system.

Table 2.3 Reference values for average planetary albedo according to [9].

Planet	Average Albedo	Albedo Range
Mercury	0.106	0.09 - 0.45
Venus	0.65	
Earth	0.30	
Mars	0.15	
Jupiter	0.52	
Saturn	0.47	
Uranus	0.51	
Neptune	0.41	

As it can be noticed from table 2.3, Earth are characterized by an average albedo of 0.3. For an orbiting spacecraft, the albedo fluctuates within the range $[0.05 - 0.6]$, respectively in open ocean and high cloud coverage/icecap conditions.

The fraction of albedo radiation absorbed by the spacecraft is:

$$Q_{\text{albedo}} = J_S\, a F_{\text{S/C-planet}}\, \alpha \qquad (2.23)$$

17

where a is the albedo factor and $F_{S/C\text{-planet}}$ is the view factor of the spacecraft surface to Earth, also called visibility factor. Earth can be modelled as diffuse reflecting sphere, in which case the visibility factor varies with the orbit altitude as shown in Figure 2.7.
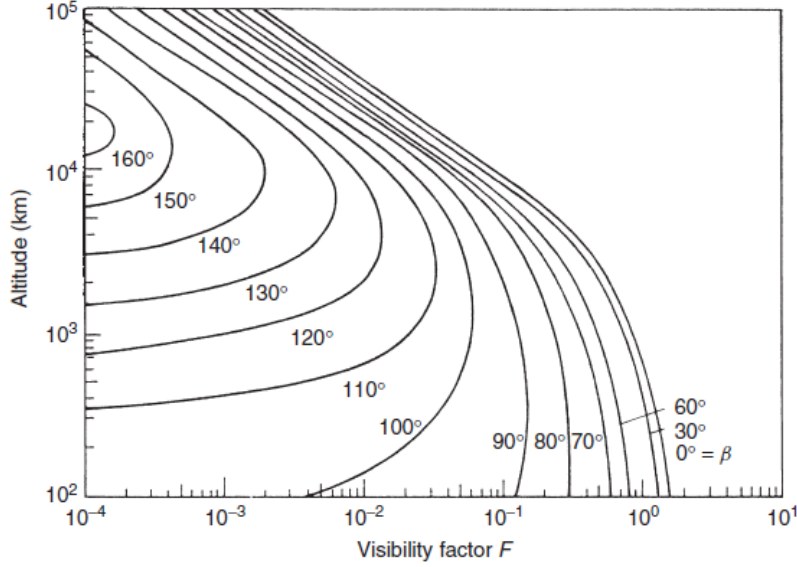
Figure 2.7 Visibility factor variation with orbit altitude. β is the angle between the local vertical and the Sun's rays.

2.2.3 Planetary infrared radiation source

All the incident light not reflected as albedo is absorbed by the planet and re-emitted to space as IR thermal radiation with a spectrum of a black body at an average temperature of 288 K. The earth IR radiation also varies across the globe but less than the albedo. It depends on factors such as surface and air temperature, atmospheric moisture content and cloud coverage. Reference values for average planetary albedo and infra-red radiation are given in table 2.4. The total IR radiation absorbed by the spacecraft is given by:

$$Q_{\text{planet}} = J_p \, A \, F_{S/C-\text{planet}} \, \varepsilon \tag{2.24}$$

where ε is the infrared absorption coefficient of the surface, whereas J_p is the planet IR heat flux, which for Earth is defined as:

$$J_p = 237 \left(\frac{R_{\text{rad}}}{R_{\text{orbit}}} \right)^2 \tag{2.25}$$

with R_{rad} the radius of the Earth's effective radiating surface and R_{orbit} the orbit radius. The constant value 237 refers to the Earth's radiating intensity (W/m^2).

Table 2.4 Reference values for average planetary infra-red radiation according to [9].

Planet	Average IR [K]	IR Range [K]
Mercury	442.0	100 - 725
Venus	231.7	737 (surface)
Earth	288.0	
Mars	210.1	184 - 242
Jupiter	110.0	112 @ 1 bar
Saturn	81.1	1 - 143 @ 1 bar
Uranus	58.2	76 @ 1 bar, 53 @ 0.1 bar
Neptune	46.6	72 @ 1 bar, 44 @ 0.1 bar

2.3   Thermal balance equation of a Spacecraft

Recalling equations (2.2) and (2.3), the energy balance relation specified for a spacecraft
is given as:

$$Q_{\text{net},i} = m_i C_i \frac{\mathrm{d}T_i}{\mathrm{d}t} = Q_{\text{out},i} + Q_{\text{in},i}$$

$$mC\frac{\mathrm{d}T}{\mathrm{d}t} = Q_{\text{Sun}} + Q_{\text{albedo}} + Q_{\text{planet}} + Q_{\text{internal}} - Q_{\text{S/C}} \tag{2.26}$$

where Q_{internal} represents the internal heat generated by the spacecraft onboard equipment
and $Q_{\text{S/C}}$ accounts for the thermal radiation emitted by the spacecraft into space. Equation
(2.26) defines the transient thermal balance equation of the spacecraft. In steady state the
(2.26) can be rewritten as:

$$Q_{\text{Sun}} + Q_{\text{albedo}} + Q_{\text{planet}} + Q_{\text{internal}} = Q_{\text{S/C}}$$

$$\alpha J_{\text{s}} A_{\text{solar}} \cos\theta + J_{\text{s}} a A_{\text{albedo}} F_{\text{S/C-planet}}\alpha + J_{\text{p}} A_{\text{planet}} F_{\text{S/C-planet}}\varepsilon + Q_{\text{internal}} = \varepsilon \sigma T^4 A_{\text{tot}} \tag{2.27}$$

If we assume that J_{s}, J_{p} and Q_{internal} remain constant, the spacecraft will reach an equilib-
rium temperature T given by:

$$T^4 = \frac{A_{\text{planet}} J_{\text{p}}}{A_{\text{tot}}\sigma} + \frac{Q_{\text{internal}}}{A_{\text{tot}}\sigma\,\varepsilon} + \frac{(A_{\text{solar}} J_{\text{s}} + A_{\text{albedo}} J_{\text{s}} a F_{\text{S/C-planet}})}{A_{\text{tot}}\sigma}\left(\frac{\alpha}{\varepsilon}\right) \tag{2.28}$$

So the spacecraft temperature is dependent on the ratio α/ε, particularly for spacecraft
having small Q_{internal} [21].

Chapter 3

Variable emissivity technology: State of the art

The heat amount exchanged by a radiator is strongly affected by both the internal heat fluxes and the thermal environment that the satellite faces. The radiator must be carefully sized in order to ensure the right dissipation in the worst hot case, namely the one dealing with maximum internal and external fluxes. However, since these two fluxes may vary considerably during the mission lifetime (i.e. electronics switch off, eclipses, attitude variation, surfaces degradation) an accurate design has to be determined in order to obtain a trade-off flexibility on the radiator performance, avoiding excessive heat rejection to space and thus overcooling of internal units.

To cope with that issue, structures implementig variable thermo-optical properties have been developed and studied in the last view years, leading to the realization of a plethora of micro and macro devices. Those engineering solutions could be divided, firstly, on the basis of the type of thermal control system and, secondly, on the basis of the nature of the phenomenum that ensures the control:

- active thermal control devices

    - electro-mechanical based devices
    - electro-chromic (ECH) based devices

- passive thermal control devices

    - thermo-chromic (TCH) / phase changing based devices
    - bimetallic, spinging actuated, louvers (venetian-blind louvers)
    - Shape memory alloys (SMAs) and multylayer composite materials self adaptable structures

3.1 Active thermal control devices

Active thermal control devices need a power input in order to fulfil their function. In the following paragraphs the most common active solutions providing variable emissivity properties are presented and briefly described.

3.1.1 Electro-mechanical based devices

Variable emissivity mechanical systems (louvers) and complex electro-mechanical systems (MEMs)[4, 14] implement hinges and actuators in order to perform simple movements. These complex, heavy mechanical devices, such as micro-machined louvers or shutter arrays [4, 14], have been studied in order to achieve thermal control by varying the effective thermal emissivity of a surface [1]. The microshutter arrays (MSAs) consist of a multitude of unit cells (figure 3.1) and are actuated by small electrostatic comb drive motors which provide linear control of the effective thermal emissivity with a turndown ratio (maximum emitted energy/minimum emitted energy) equal to 5 [1, 6]. MEMs and MSAs require the application of an external bias voltage close to 1000 volts for MEMs [4] and close to 20 volts for MSAs [15], thus consuming electrical power.

(a)   (b)
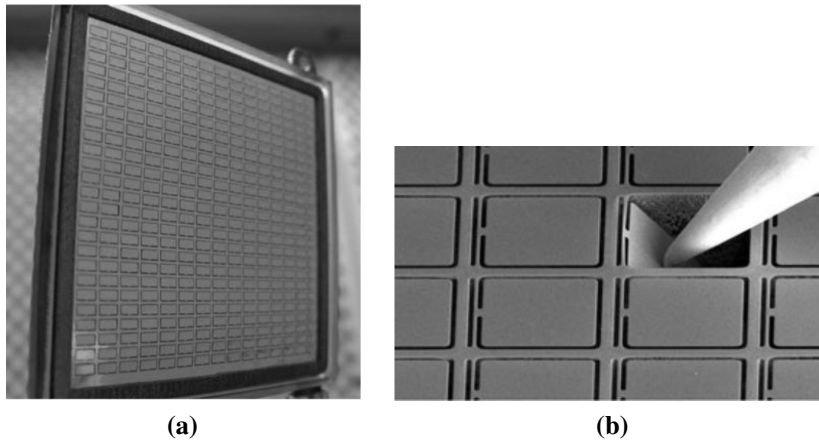
Figure 3.1   Micro louvers (a) [4] and close up of micro-shutters (b) installed on the JWST [15].

3.1.2 Electro-chromic (ECH) based devices

Lighter solution is represented by electrochromic (ECH) device technology. ECH devices for spacecraft thermal control applications are based upon materials that are able to alter their reflectance in the infra-red wavelengths in response to changes in an applied bias voltage ($\pm \sim 1\,V$) [3, 19]. Their operation relies upon a chemical reaction of oxidation or reduction due to charge migration within the electrochromic material, leading to either a collection or removal of electrons [19]. A radiator coated with an electroactive

material offers the same variable-emittance performance as a mechanical louver along with decreased mass, cost, and mechanical complexity [19]. Typical variation in the IR emissivity of these devices is in the range from 0.3 to 0.75, with a maximum $\Delta\varepsilon$ of 0.55 [19]. Researchers at the Jet Propulsion Laboratory (JPL) and Ashwin-Ushas Corporation are working to develop electrochromic device technology for use on a microspacecraft application funded by NASA's Exploration Systems Mission Directorate (ESMD) and based upon a pre-cursor project at JPL (the Low Cost Adjunt Microspacecraft or LCAM) [19].

Another promising approach is represented by electrically switchable broadband infrared reflectors based on polymer stabilised cholesteric liquid crystals. The IR reflectors are able to change their reflection/transmission properties through the application of an electrical voltage [1].

3.2 Passive thermal control devices

In the space field, where the mass and power saving is the most important driving requirements, passive thermal control solutions are by far the preferred choice. Although, passive solutions do usually not provide comparable performance against active thermal control devices for spacecraft and conditions with high demanding requirements (i.e. cryogenic cooling, long eclipses, long phases with direct sun-light exposure, etc.). In recent years many efforts have been made by researchers in order to overcome those limitations, leading to the development of innovative technologies with improved performance based on material's phase transformation and microstructural rearrangements.

3.2.1 Thermo-chromic (TCH) / phase changing based devices

A recent promising approach to provide variable emittance comes from the use of thermochromic (TCH) materials. Many studies have being done so far on vanadium dioxide (VO_2), which presents an anomalous thermal emittance profile that is strongly correlated with temperature. VO_2 has a metal-insualator transition temperature (T_{MI}) at $63°C$ [13]. The metal-insulator transition is associated with an optical transition in the IR range. Indeed, VO_2 has a two-way behaviour towards IR radiation: at $T < T_{MI}$ it is IR transparent and at $T \geq T_{MI}$ it becomes IR reflecting [13]. This peculiar property of vanadium dioxide provides a filter against the energy in the solar spectrum with a maximum contrast at $2.5\,\mu m$ [13]. Even though VO_2 is relatively easy to synthesize and process, many efforts are needed to make its transition temperature stable around room temperature [13]. The $R_{1-x}M_xMnO_3$ perovskites offer good compromise with simple synthesis method and sharp metal-insulator transition [13]. These materials are *colossal magnetoresistance* (CMR) manganites and they are based on the ABO_3 perovskite structure shown in figure 3.2. The most widely used are characterized by the chemical formula $R_{1-x}A_xMnO_3$ (where R is a

23
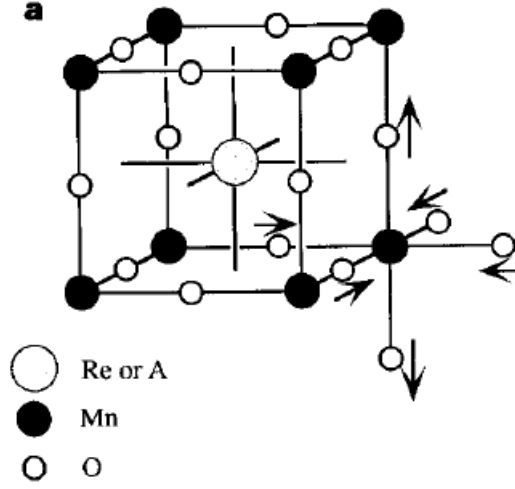
Figure 3.2 Crystal structure and electronic structure of the manganite pervoskite [18].

rare earth such as *La* or *Nd*, and *A* is a divalent alkali, namely *Sr* or *Ca*) [18]. Actually, also the CMR manganites present limitations. Indeed, they exhibit abrupt metal-insulator transition at 150 and 180 K, but the T_{MI} remains low for applications [13].

An alternative to VO_2 in the development of variable thermal emission devices is represented by the phase changing material $Ge_2Sb_2Te_5$ (GST) [8]. The emissivity of this thermal emitter is switchable, tunable and wave-length-selective. The wave-length se-
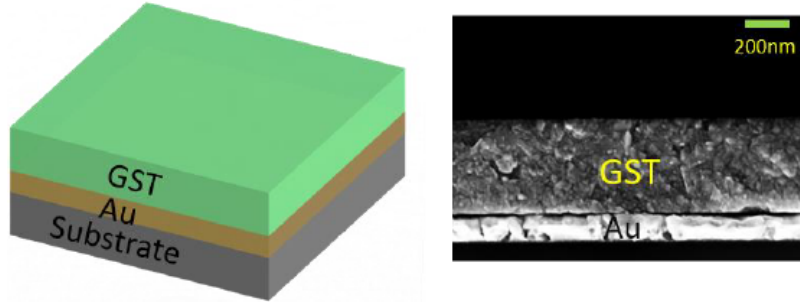
Figure 3.3 3D schematic of the thermal emitter composed of a GST film on top of a gold film (on the left) and a SEM image of a cross-section of the fabricated thermal emitter (on the right).

lectivity (in the range [3 - 15]μm]) is accomplished by altering the GST thickness. The switchable thermal emission is achieved by transforming the GST between amorphus and crystalline phases. Finally, the emissivity of the thermal emitter can be continuosly tuned by controlling the proportions of amorphus and crystalline molecules of GST [8]. When

the GST is at the crystaline phase, the emissivity approaches the ideal blackbody maximum value (on state), while the emissivity is suppressed to below 0.2 (off state) at the amorphus phase [8]. The fabrication process involves simple GST film deposition on top of a metal film (figure 3.3).

3.2.2 Bimetallic, spinging actuated, louvers (venetian-blind louvers)

A modern "Flight Proven" application of passive thermal control system is represented by the Rosetta mission: this probe was orbiting its target Comet 67P/Churyumov-Gerasimenko, whose orbit reached its closest point to the Sun on 13 August 2015. The rendezvous required a decade-long odyssey of planetary flybys and wide temperature fluctuations. In certain points Rosetta urgently needed to dump waste heat, while in other cases heat became essential to keep the mission from freezing during its 31-month hibernation phase. The solution adopted consisted of a particular louver radiator (see figure 3.4), with a plethora of reflective metal blades. In high temperature conditions they remain open to reject heat towards space by radiation, on the contrary, in cold cases they automatically close up. The louvers rely on a passive aperture mechanism of blades. The active surfaces are moved by coiled springs made up of a trio of different metals that expand and contract at different rates, precisely tailored to rotate as required.
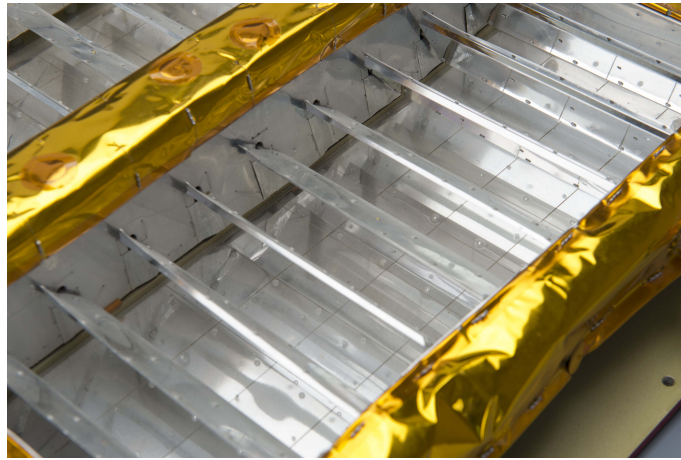
Figure 3.4   Passive thermal louvers application to Rosetta mission.

3.2.3 Shape memory alloys (SMAs) and multylayer composite materials self adaptable structures

In recent years, the use of technologies and materials based on the imitation of biological systems is becoming more and more predominant in engineering. In the space sector, the biomimetic approach is used as an innovative engineering tool for future space missions

applications and its study focuses the attention to understand the mechanisms used in nature [17, 23]. In this context, bioinspired materials featuring complex movements (figure 3.5) as pure imitation of plants behaviour have been developed [1] and studies on the application for a smart spacecraft thermal control are ongoing [20].
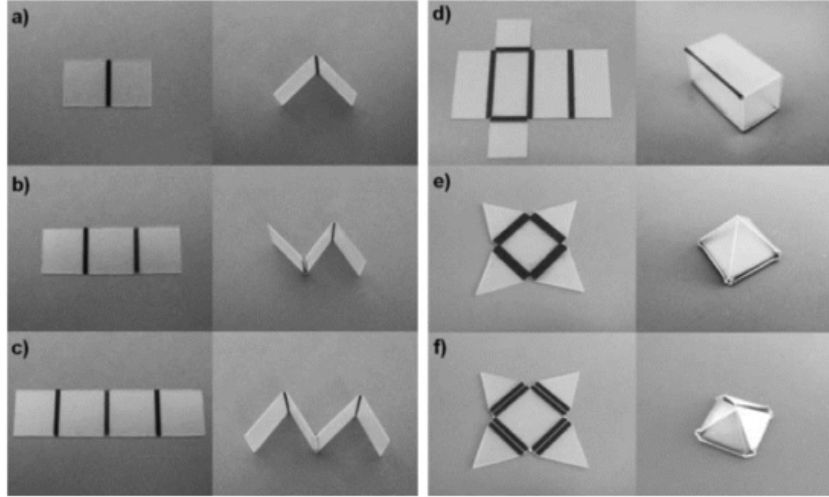
Figure 3.5   3D structers with self-shaping capabilities of shape memory polystyrene film patterned.

Materials that are capable of changing their shape are the well-known shape memory alloys (SMAs) and the exotic shape memory polymers (SMPs) [1], as well as temperature sensitive hydrogels [11]. SMPs and SMAs behaviour relies upon phase change of the material at micro scale caused by external environmental stimuli. Morphing radiators are developed based on a technology that employs the shape memory behaviour of Nitinol in conjunction with a bias load to actuate the surface of the radiator [5]. The basic function of this new concept is illustrted in figure 3.6.

(a)   (b)
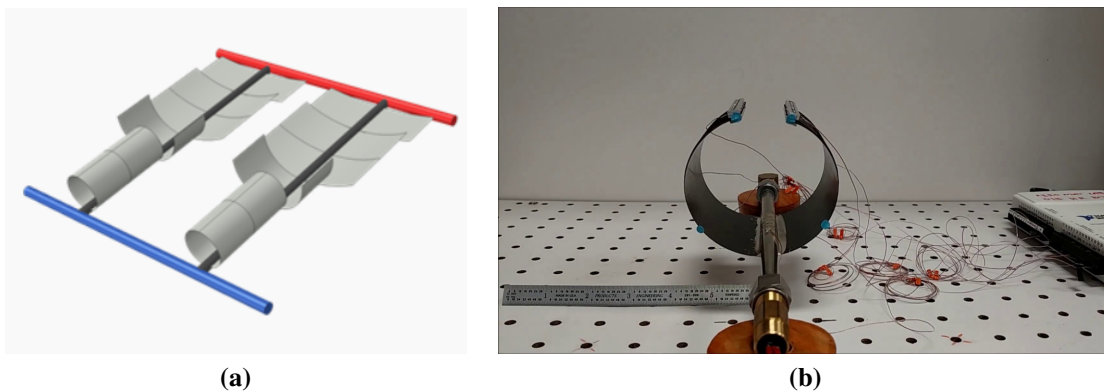
Figure 3.6   Conceptual scheme of the morphing radiator (a) and its experimental setup (b).

The shape memory alloy (SMA) presents a two-memory behaviour according to the temperature of the facesheet. In hot conditions, the radiator will take its fully extended austenitic shape, exposing to space its top high emissivity surface. In cold conditions, the radiator will transform in its deformed martensitic shape, exposing to space its bottom low emissivity surface. In this way, the variation of the view factor of the radiator to environment provides a selective surface emissivity and it is possible to produce very high turn-downs ratios capable of enabling single-loop thermal control of a vehicle using propylene-glycol or similar non-toxic, high freezing-point working fluids [5].

SMA materials are also used for the construction of artificial flowers [16], as it is the case of figure 3.7. This self-shaping structure consists from a peduncle in thermal and mechanical contact with the spacecraft radiator panel. When the sun irradiates the flower and/or the radiator temperature exceed a predetermined limit, the SMA actuators in the ribs bend causing the flower to open (figure 3.7). Therefore, the flower exposes to space its
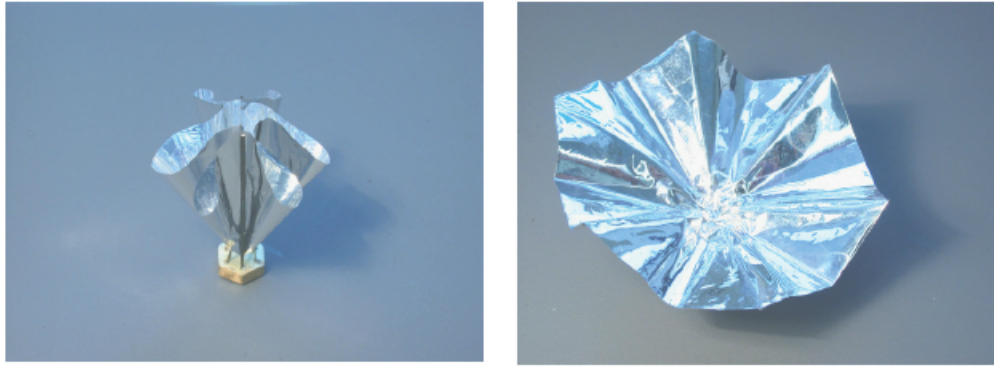
Figure 3.7 On the left side the artificial flower in closed configuration. On the right side the flower in fully opened mode.

highly reflective surface preventing the radiator to overheat. The peculiar property of this system is the absence of any friction-kinematic movements, thus providing high reliability of the device compare to mechanical louvers [16]. However, a problem due to the intrinsic mechanism of deployment deals with a wide inter-device gap which drastically decreases the efficiency of the whole system.

Self-shaping structures can be obtained also through the superposition of different materials with dissimilar coefficients of thermal expansion (CTE). [1] proposed an innovative solution based on the development of a new generation of multifunctional materials with variable thermo-optical properties. The bioinspired structures are a priori tuned to passively respond to external temperature stimuli by changing their geometry and their material exposure thus either absorbing/emitting or reflecting thermal radiation accordingly. The coefficient of thermal expansion (CTE) mismatch between two fibrous anisotropic

layers, creates shape memory materials which alter their shape via the developed internal stresses [1]. Thus, the self-shape materials start to transform themselves by the temperature deviations and through the large CTE of the anisotropic multilayer material. The behaviour of these materials are similar to bi-metallic strips one, but they are also capable to combine either bending and twisting movements, thus allowing to perform very complex modes [1, 23]. The resulting advantages are light "shape memory materials" that
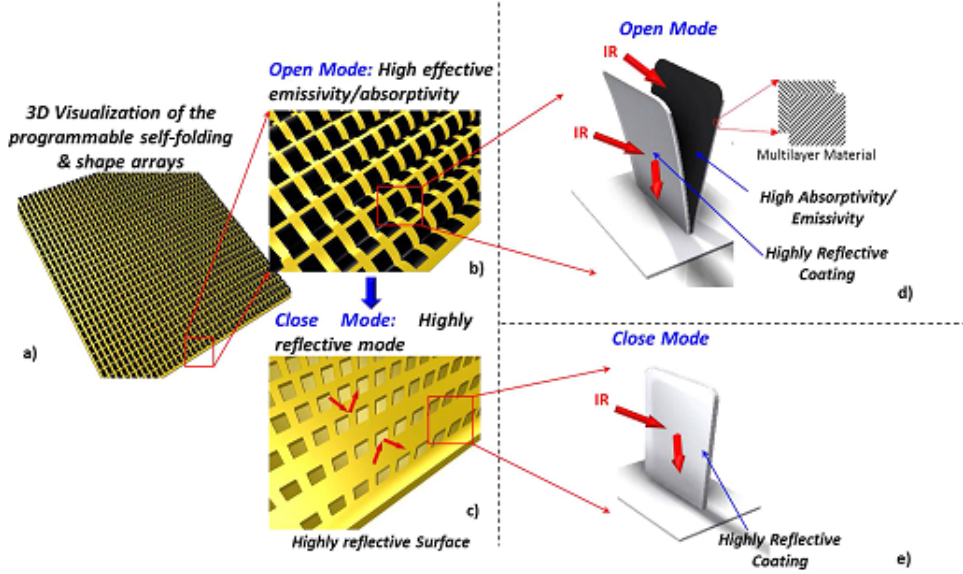
Figure 3.8 3D schematic diagramm of the programmable self-shape arrays operating behavior.

passively react to a very broad range of thermal requirements ($-200°C$ to $350°C$) [1], which cannot be achieved by SMPs and SMAs. Therefore, the self-shaping capabilities via microstructural rearrangements of those adaptable arrays represent an innovative and smart way of providing thermal regulation for earth and space applications.

Chapter 4

Smart Self-Shape Radiator: properties and design

According to what mentioned in chapter 3, the most promising track to passive thermal control based on variable emissivity properties seems to be represented by dynamic adaptable materials that self-shape as a reaction to surrounding temperature stimuli. This disruptive technology would provide a significant impact on the thermal control design of satellites that will be involved in future scientific and interplanetary missions. Thanks to no need of power input in order to realize the thermal control, the bioinspired self-shape material [1] provides a lighter weight, simpler and cheaper solution than classical macro and micro electromechanical louvres. In the present chapter, attention is being focused on the description of the thermal concept design, the intrinsic mechanism of actuation, the structure and fabrication process of the self-shaping material for the realization of an innovative smart spacecraft radiator with variable thermal emissivity.

4.1   Thermal behaviour

The radiative behaviour of a body could be instantaneously altered via: i) the change in its emissivity coefficient (ε), absorptivity (a), reflectivity (ρ) and transmissivity (τ); ii) the view factor of the body's geometry [1]. The self-shape structures proposed by [20] and [1] are dynamic structures (fins) capable of reacting under temperature deviations, presenting variable and programmed thermal emissivity behaviour. The smart surfaces imitate the complex behaviour of certain plants that change their shape when in need to absorb more or reject excess sunlight. The transformation of these "bioinspired materials" provides a passive way to manipulate thermal radiation without the need of electrical power consumption. The energy required for their activation comes from the environment. The transformation of the responsive fins conceals (closed geometry) or reveals (open geometry) one of the materials and regulates the view factor of the patterned surfaces, thus enabling the realization of a variable and programmable effective thermal emissivity ($\varepsilon_{\max}$) [2]. In

figure 4.1 is shown a prototyping model. The radiator with variable emissivity properties
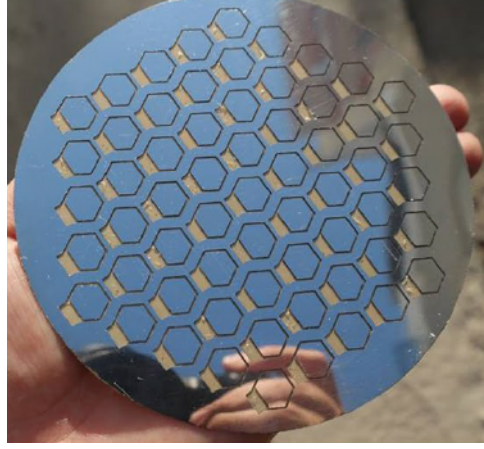
Figure 4.1 Sample of an array implementing bioinspired self-shape structures. Courtesy image of N. Athanasopoulos [2].

proposed by [20] consists of a main surface with high emissivity material (ε_H) on the top of which are placed dynamic self-shape structures made with two different thermal finishes. The internal surface is characterized by the same high emissivity material of the main surface radiator, while the external surface is made of a low emissivity material (ε_L). The self-shape fins are programmed to have a two-way memory (Figure 4.2). At an initial temperature (T_{m1}) they morph into a full closed geometry that completely cover the radiator surface, thus exposing only the high emissivity coating. At a second defined temperature level ($T_{m2} > T_{m1}$) the adaptable structures transform themselves into a full opened geometry revealing the internal high emissivity material. In this way, the
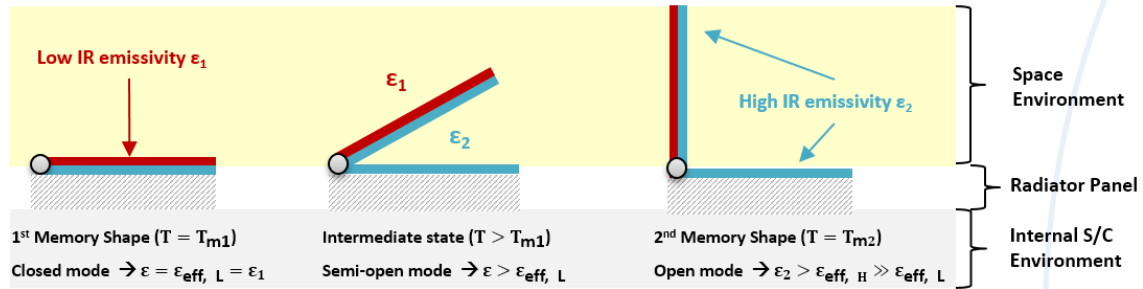
Figure 4.2 Self-shape array thermal concept design [20].

dimensions of the cavity are increased as the temperature rises. When the self-shape structure assumes its first memory at T = T_{m1}, the value of its effective emissivity (ε_{eff-L}) coincides with that of the external low emissivity coating (ε_1) and the area of the cavity is nullified. As long as the temperature increases, the structure starts to transform and, when it reaches the second memory temperature value (T_{m2}), it opens completely assuming its

maximum value of effective thermal emissivity ($\varepsilon_{\text{eff}-\text{H}}$), which is lower than that of the internal material coating (ε_2) because the presence of the fin reduces the view factor of the underneath plain surface by partially shading it.

As it can be seen from Figure 4.3, the patterned surface can assume states from closed to open or vice versa in the range of temperature $30.4\,^\circ\text{C} \leq \text{T} \leq 80.2\,^\circ\text{C}$. In cold cases, the patterned surface has a global low emissivity value, thereby limiting the heat flux rejected towards the environment. When the temperature increases, the fins starts to transform and their high emissivity value dominates. As the fins open wider and wider, the ability of the surface to radiate energy drastically increases. The behaviour of such bioinspired respon-
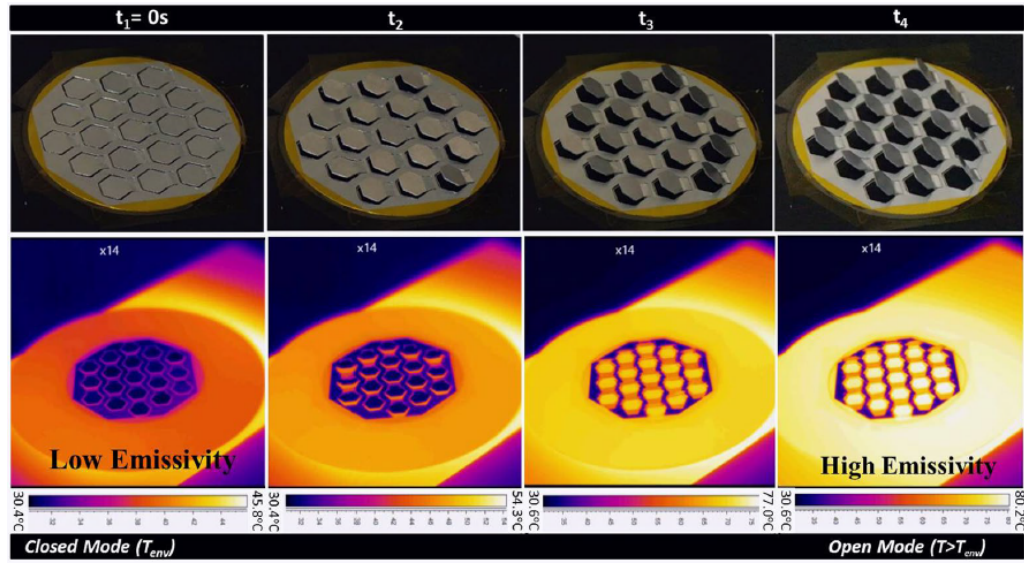
Figure 4.3   Smart patterned surface with two-way memory behaviour ensuring variable and programmable emissivity properties. Courtesy image of N. Athanasopoulos [2].

sive structures could be directly transferred to space technology (e.g. radiators) for a more efficient thermal control. According to the illustration provided by Figure 4.2, in cold cases, the smart array causes the radiator area to have low emissivity properties, thereby reducing the heating power needed for spacecraft survival with increasingly effectiveness on battery mass savings. Whereas, in hot situations, the smart fins fully open providing the radiator with a wide high emissivity area, allowing for efficient heat dissipation [20]. In conclusion, a surface which incorporates self-shape structures can be designed to quickly absorb radiative heat energy at low temperature levels, but simultaneously is capable of passively controlling its maximum temperature in order to prevent overheating [1].

4.2   Mechanical behaviour

The transformation of the fins is the "driving force" in accomplishing the variation of the radiator's thermo-optical properties. These high responsive materials undertake extremely large deformations based on the mismatch of the coefficient of thermal expansion (CTE) between the anisotropic layers of the multilayer structure. As the generic fin is stimulated by an external temperature load, the material experiences the development of internal stresses which generate either bending and twisting out-of-plane moments. The large mechanical deformation is responsible of the shape alteration of the fin, forcing it to be in open mode in higher temperatures, whereas the first memory shape starts being recovered in temperatures lower than T_{m2}.

The effective emissivity of the bioinspired structures is affected not only by the emissivity of the outer (ε_1) and inner (ε_2) material, but it depends also from the geometry of the unit-cell which is a function of the following physical and mechanical characteristics of the anisotropic material:

- modulus of elasticity of the two principal directions (E_1, E_2);

- Poisson ratios (v_1, v_2);

- shear modulus (G_{12});

- ply orientation (ϑ) of each layer;

Moreover, the temperature (T) represents another key parameter in the geometry definition of the fin, because it is strictly related to the gap (w) between the layers of the self-shape material (Figure 4.5). The displacement (w) of the fin represents the macroscopic result of the microstructural rearrangement of the multilayer self-shape material in response to the temperature deviation. Indeed, the adjacent ply of a different ply angle will restrict the adjoining ply in deforming freely. As a consequence, the enforced common deformations produce residual stresses within the individual plies of a laminate, preventing them from individually deform freely [1].

When the surface rejects heat, the temperature of the surfaces decreases, which leads to the reduction of the gap (w) due to the internal developed thermal stress and microstructural rearrangements. On the contrary, when the surfaces absorbs energy, the temperature increases and the gap (W) becomes wider and wider until it reaches its maximum value ($w_{m2} = w_{max}$), leaving exposed only the material with the highest emissivity value ($\varepsilon_1 = \varepsilon_H$).

The displacement (w) of the self-shape fin can be evaluated by taking in consideration the classic mechanics of composite materials. The generic self-shape surface is described through the Kirchoff-Lowe's plate model (Figure 4.4), in which the following assumptions are considered:

1. The plate is constructed with an arbitrary number of layers of orthotropic material perfectly bonded together;

2. the layers have constant thickness;

3. the material of the layers obeys Hooke's law and is transversely isotropic;

4. the transverse displacement (w) is independent of the z coordinate, i.e. ε_z is negligible;

5. the in-plane displacements u and v are assumed to be linear functions of the z coordinate, i.e. they are linearly distributed through the thickness of the plate;

6. the transverse shear strains γ_{xz} and γ_{yz} are assumed to be negligible (Kirchoff's hypothesis);

7. the plate displacements are small compared to the plate thickness;

8. the plate in-plane strains are small compared to unity.

According to assumptions 5 and 6 and indicating with apex 0 the variables referred to the mid plane, the displacement field yields:

$$u(x, y, z) = u^0(x, y) - z\, w^0_{,x}(x, y) \tag{4.1}$$

$$v(x, y, z) = v^0(x, y) - z\, w^0_{,y}(x, y) \tag{4.2}$$

$$w(x, y, z) = w^0(x, y) \tag{4.3}$$
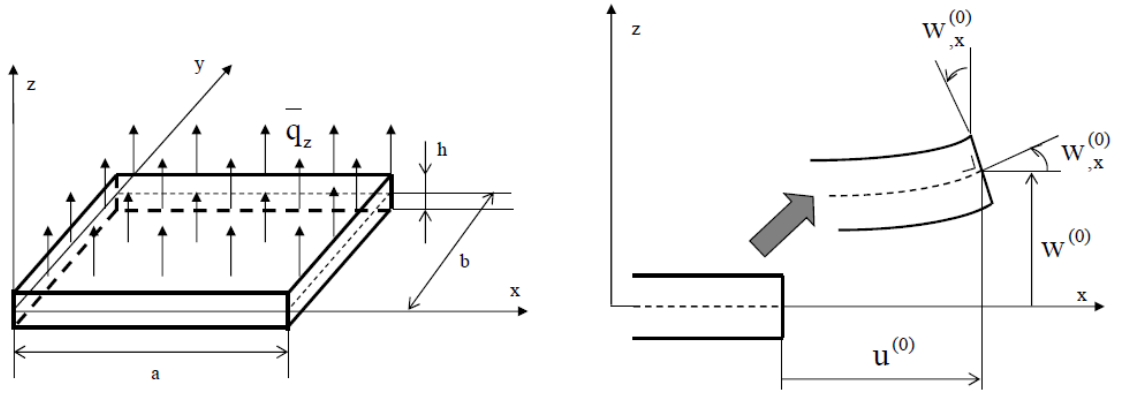
Figure 4.4   Scheme of Kirchoff-Lowe's plate model.

Therefore, the correspondent strain field in matrix notation is written as:

$$\varepsilon = \varepsilon^0 + z\, k \tag{4.4}$$

33

with (ε^0) the vector of membrane strains and ($-z\,k$) the vector of bending strain. Taking into consideration the temperature parameter, equation (4.4) is transformed to:

$$\varepsilon = \varepsilon^0 + z\,k - \varepsilon^T \tag{4.5}$$

where (ε^T) is the temperature induced deformation. Thus, the material residual stress is equal to:

$$\sigma = Q\,\varepsilon = Q\left(\varepsilon^0 + z\,k - \alpha\,\Delta T\right) \tag{4.6}$$

where (Q) is the reduced stiffness matrix, (z) is the section thickness, (k) is the vector of midplane curvatures, whereas (α) and (ΔT) are the coefficient of thermal expansion and the temperature difference, respectively. The residual force and moment intensity on the anisotropic layers are obtained by integrating, respectively, the residual stress and the product of the residual stress with the moment arm (z), over the thickness of each layer. The resulting force intensities and moments of the multilayer plate can be expressed by equations (4.7) and (4.8):

$$N = A\,\varepsilon + B\,k - \int Q\,\alpha\,\Delta T\ dz = \int \sigma\ dz \tag{4.7}$$

$$M = B\,\varepsilon + D\,k - \int Q\,\alpha\,\Delta T\,z\ dz = \int \sigma\,z\ dz \tag{4.8}$$

where:

$$A_{ij} = \sum_{n=1}^{N} \left(z_n^+ - z_n^-\right) (Q_{ij})_n = \sum_{n=1}^{N} h_n\,(Q_{ij})_n \qquad \text{membrane stiffness matrix} \tag{4.9}$$

$$B_{ij} = \sum_{n=1}^{N} \left(\frac{\left(z_n^+\right)^2 - \left(z_n^-\right)^2}{2}\right)(Q_{ij})_n \qquad \text{coupling stiffness matrix} \tag{4.10}$$

$$D_{ij} = \sum_{n=1}^{N} \left(\frac{\left(z_n^+\right)^3 - \left(z_n^-\right)^3}{3}\right)(Q_{ij})_n \qquad \text{bending-torsion stiffness matrix} \tag{4.11}$$

The plate constitutive equations, in matrix form, can be expressed by the following equation:

$$\begin{Bmatrix} N \\ M \end{Bmatrix} = \begin{bmatrix} A & B \\ B & D \end{bmatrix} \begin{Bmatrix} \varepsilon^0 \\ k \end{Bmatrix} \tag{4.12}$$

The (4.12) is a system of linear equations which can be solved in terms of strain values ($\varepsilon_x, \varepsilon_y, \varepsilon_{xy}$) and curvatures ($k_{xx}, k_{yy}, k_{xy}$), which lead to the prediction of the final shape

of the self-shaped structure. Furthermore, the out of plane displacement (w), Figure 4.5, can be calculated trough the equation:

$$w(x, y, T) = \int_{x_1}^{x_2} \int_{x_1}^{x_2} k_{xx}(T) \, dx + \int_{y_1}^{y_2} \int_{y_1}^{y_2} k_{xy}(T) \, dx \, dy$$

$$w(x, y, T) = -\frac{1}{2} \left(k_{xx}(T) \, x^2 + k_{yy}(T) \, y^2 + k_{xy}(T) \, xy \right) + \alpha \, x + \beta \, y + \gamma \tag{4.13}$$

The area of the high emissivity gap can be calculated from equation (4.13):

$$A(T) = l \cdot w(x, y, T) \tag{4.14}$$

where (l) is the width of the unit cell and (α, β, γ) are constants that can be determined through the imposition of particularly mechanical boundary conditions. Once all the material's geometrical characteristics are known, curvatures can then be calculated as a function of temperature and then high and low emissivity regions can be determined [1].
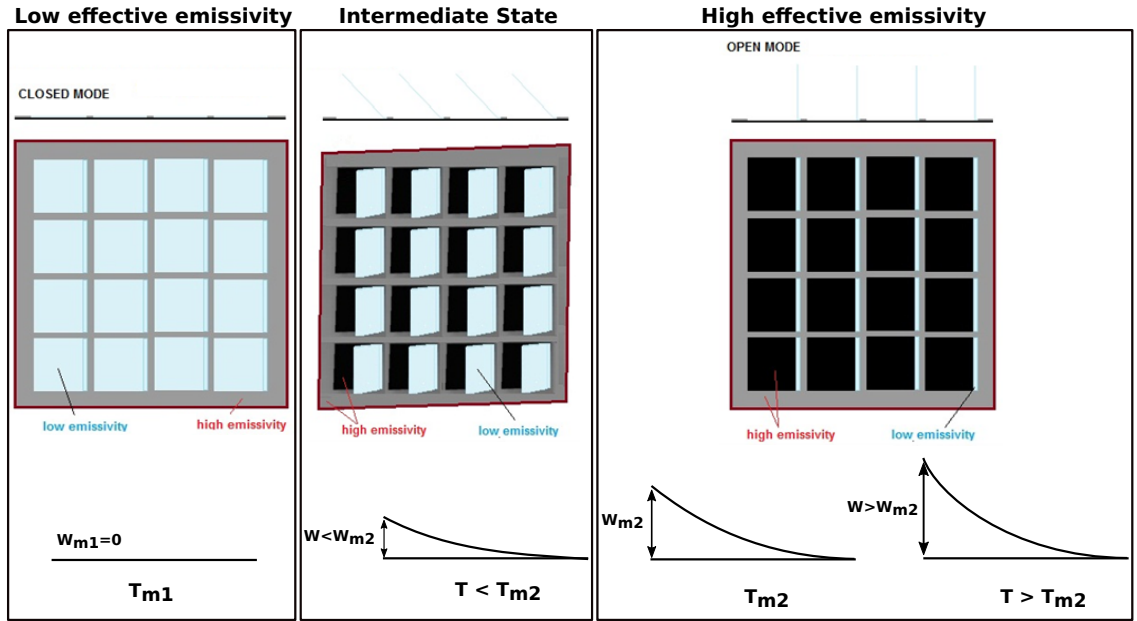
Figure 4.5   Plan view of the mechanism of actuation of the self-shape structures in pure bending mode.

The described physical behavior allows to program the activation of the smart structures in proportion to the stimulus (i.e. temperature or radiated heat flux) in a way similar to the "4D-biomimetic materials" [2]. Despite bimorph metallic layers that can perform only bending movements, the use of such anisotropic multilayer materials allows to create multifunctional structures that are able to perform pure bending, pure twisting or complex

combined modes [1]. Therefore, bioinspired self-shape materials based on fibrous composite laminates could be an enabling technology in aerospace industry, where reliability and multifunctionality have reached more and more emphasis in recent years [12]. Active materials can effectively reduce the complexity of a system, providing a more compact arrangement and thus leading to higher overall reliability, especially at low cycles [12].

4.3   Material structure and fabrication

The development process of these particular shape memory materials is extremely versatile and could be performed via low cost techniques, namely:

- Multi-layered fibrous anisotropic materials

- Anisotropic nanocomposites

- Nano-reinforced multilayer hydrogels

- Particular micro-structure with anisotropic properties

With regard to the research work conducted by Athanasopoulos [1], the self-shape material selected for our application is a multilayer carbon fiber/epoxy composite made of two layers of 125 μm thickness. The composite layers are sandwiched between a black coating ($\varepsilon_1 = 0.95$), applied on the internal surface of the fin, and an aluminum foil layer (20 μm thickness and $\varepsilon_2 = 0.075$), attached to the external side of the fin. The contact between the multilayer composite material and the two coatings is guaranteed through the use of an adhesive particularly suited for low-energy plastics application (Methacrylat- & Amine-based resins) mixed with 1% multi-walled carbon nanotubes ($\varepsilon > 0.9$). Figure 4.6 illustrates the sequence of materials and layers used by Athanasopoulos [2] to develop the smart patterned surface and summarized in Table 4.1.

Table 4.1   Material composition of the multilayer self-shape surface at different regions.

Deformable Region	Non-deformable Region	Deformable or Non-deformable Region
Oriented polyethylene (PE)	Aluminium substrate	Oriented polyethylene (PE)
Adhesive	Graphite coating	Adhesive
Aluminium strips	Oriented PE	Aluminium strips
Aluminium film (5 μm)	Aluminium strips	Adhesive
	Aluminium film	Polished Aluminium
	Adhesive	
	Polished Aluminium	
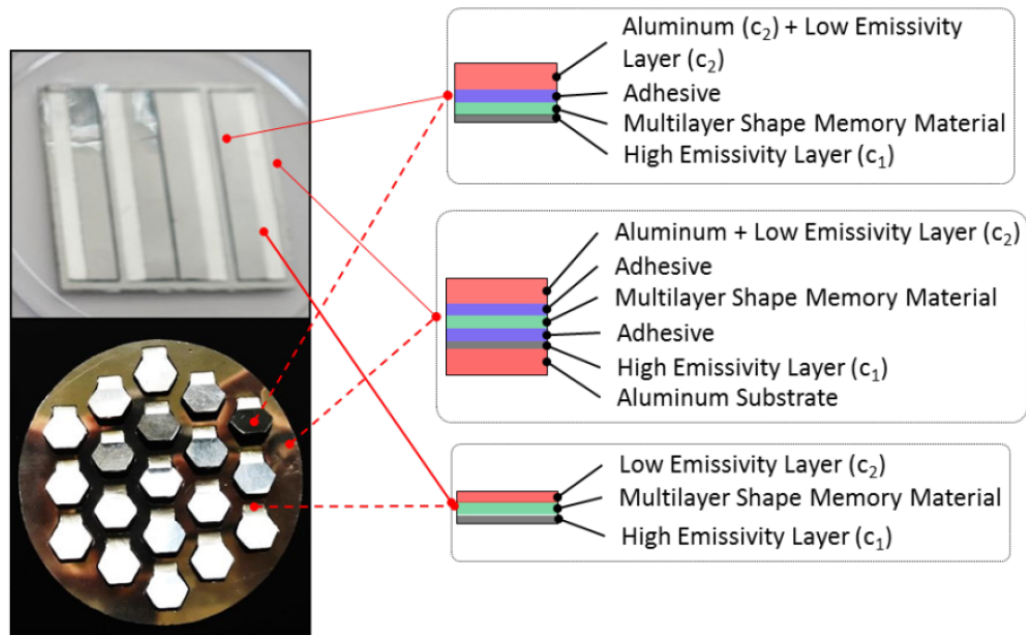
Figure 4.6 Stacking sequence of the materials and layers for the array multilayer structure. Image courtesy of Athanasopoulos [2].

A cross section of the composite material is presented in Figure 4.7.
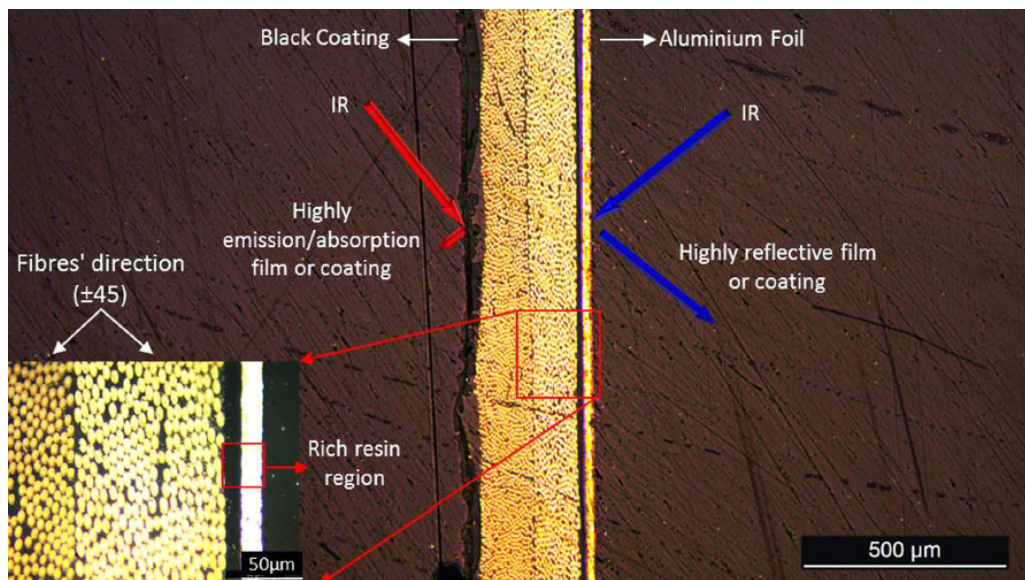
Figure 4.7 Detail of the cross section of the multilayer structure made of the three different materials: black coating/-45/+45/aluminium foil [2].

The material structured presented in this section is an example of how inexpensive "shape

memory materials" can be developed to passively react to a wide range of temperature ($-200\,^{\circ}\mathrm{C} \div 350\,^{\circ}\mathrm{C}$), which cannot be achieved by the more exotic SMPs and SMAs. Multilayer anisotropic composites act similarly to SMAs and SMPs, because of their attitude to apparently recover their original shape in response to environmental stimuli. However, this sort of memory shape property does not rely on the noticeable Shape Memory Effect (SME), which is triggered by solid-solid phase transformation, but it is due to the purely mechanical tailoring of the fibrous composite material that, coupled with temperature loads, generates internal stresses and thus the global deformation of the multilayer structure.

4.4 Thermal design optimization

The programmed behaviour of the bioinspired structures can be achieved trough the shaping transformation, by regulating the view factor and the material that is exposed to the environment [1]. The variation of the geometry of the fins conceals or reveals one of the materials, creating a surface with tunable and programmable effective thermal emissivity [1]. As it has been discussed in section 4.1, the material's physical and mechanical properties as well as the materials which alternate in the exposure to the environment affect the radiative properties of the smart surface. However, the shape of the fin, their size and their spatial distribution causes them to interact with each other. Therefore, their combination and interaction determine the global response of the surfaces, thus enabling their *a priori* design [2].

The aim of the present chapter is to execute a preliminary sizing of the smart taper that will be tied on the top of the radiator and to maximize its radiative performance in both cold and hot conditions. The chapter is divided into two main sections according to the two optimization criteria that are employed:

- minimization of the high emissivity area of the array in Cold Case (i.e when fins are completely closed);

- maximization of the radiative conductor (GR) of the overall array in Hot Case (i.e. when fins are completely open).

4.4.1 Cold Case: minimization of the radiator high emissivity area

In Cold Case conditions, especially during long eclipse phases, the spacecraft is subjected to the minimum environmental heat fluxes. Therefore, the temperature of the internal units drastically decreases and so, the thermal control subsystem has to maintain each component within its survivable temperature range. Radiators are typically sized in worst hot case, in order to be able to reject to space the maximum heat flux, while preventing the overheating of spacecraft internal units. As a result, in cold cases, classical radiators tend to dissipate too much energy, thus compromising the efficiency of the overall spacecraft.

With the programmed self-shape radiator we want to reduce the risk of undercooling of spacecraft's internal units in Cold Case, by minimizing the high emissivity area of the radiator.

Once the combination of materials (colours) on the fins are defined, the problem becomes purely geometric and its solution is a merely function of:

- the shape of the fins;

- the size of the fins (H_f);

- the distance between the self-folding structures (w_f);

- the distance between the fins and the boundary sides of the radiator (δ_b).
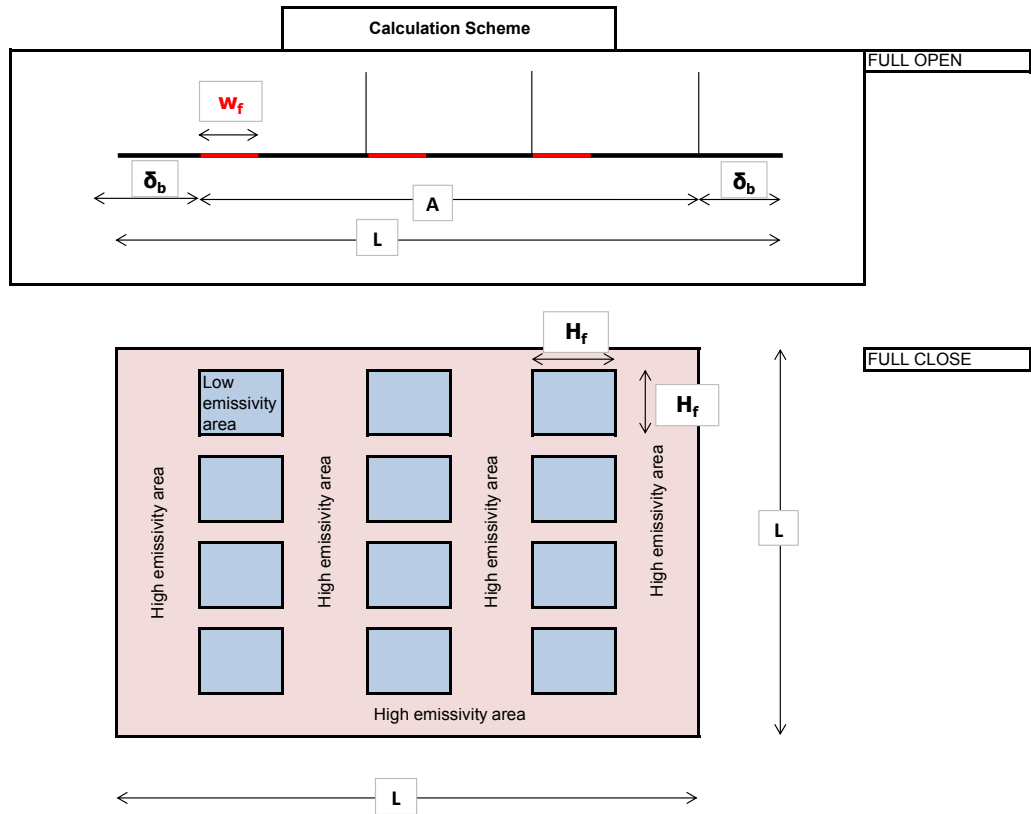
Figure 4.8   Calculation scheme for the thermal design optimization.

We decide to design the radiator as an assembly of various 200x200 mm arrays with square fins all oriented in the same direction. The number of arrays employed depends on the

dimension of the radiator that we want to mounted on the spacecraft. As a result, the design variables reduced to the number of three, namely (H_f), (w_f) and (δ_b).

For this purpose, it was developed a user-defined algorithm based on parametric approach, that allows to evaluate the percentage of high emissivity radiator area by studying different fins configurations in terms of (H_f), (w_f) and (δ_b). From the calculation scheme illustrated in Figure 4.8, the objective function to be minimize is given by the equation (4.15):

$$A_{\varepsilon_H} = \frac{\left[L^2 - (N_f \cdot H_f)^2\right]}{L^2} \tag{4.15}$$

$$N_f = \frac{[(L - 2\delta_b) + w_f]}{(H_f + w_f)} \tag{4.16}$$

where (N_f) is the number of adaptable fins for one strip and it is in turn a function of (H_f), (w_f) and (δ_b). Therefore, the total number of adaptable structures within a 200x200 mm array is evaluated as $N_{tot} = N_f \mathrm{x} N_f = N_f^2$. This is derived from the squared geometry assumed for the array studied.

We select the three configurations that gives the lowest values for A_{ε_H} with an integer number of total fins (N_{tot}), see Table 4.2.

Table 4.2   1st optimization criterion: selected configurations for a 200x200 mm array.

L [mm]	H_f [mm]	δ_b [mm]	w_f [mm]	A [mm]	N_{tot} [mm]	A_{ε_L} %	A_{ε_H} %
200	3	0.5	0.5	199.0	3249	73.1	26.9
200	6	0.2	0.9	198.2	1024	92.2	7.8
200	10	1.0	1.5	197.0	324	81.0	19.0

4.4.2   Hot Case: maximization of the overall GR of the radiator

In Hot Case the radiator has to dissipate the widest amount of heat, in order to prevent internal units from overheating and to avoid possible damages to the spacecraft. When the fins are completely open, the main panel of the spacecraft radiator reveals to space the high emissivity material (ε_H). However, the presence of moveable structures reduces the view factor of the radiator towards space compare to a traditional flat one, because each fin shades the neighbouring fin. The size of the self-folding structures and the distance between each other play a relevant role in the view factor. So, it is important to verify for all the three configurations selected in Table 4.2, which one maximizes the view factor of

the overall array. Since the radiative analysis are made with the use of the thermal software package ESATAN-TMS, it is useful to refer to the radiative conductor (GR) instead to the view factor (GV). The radiative heat flux between the element i and the element j may be expressed by the formula:

$$q_{i,j} = \sigma \, \varepsilon_i \, \alpha_j \, A_i \, GV_{i,j} \cdot \left(T_i^4 - T_j^4 \right) = \sigma \cdot GR_{i,j} \cdot \left(T_i^4 - T_j^4 \right) \tag{4.17}$$

and therefore:

$$GR_{i,j} = \varepsilon_i \, \alpha_j \, A_i \, GV_{i,j} \tag{4.18}$$

Where σ is the Stefan-Boltzmann constant, ε_i is the emissivity of element i, α_j is the absorptivity of element j, A_i the radiating surface of element i, $GV_{i,j}$ the view factor between the elements i and j.

The self-shape array is modelled in ESATAN-TMS by creating a single unit cell and then replicating it along the two spatial dimensions x and y. Each unit cell has an internal white painted surface ($\varepsilon_H = 0.9$), while the upper side is aluminized ($\varepsilon_L = 0.035$). The radiator surface on top of which are applied the unit structures are white painted ($\varepsilon_H = 0.9$). We assume a linear fin aperture variation as function of radiator surface temperature [20]. Figure 4.9 represents the geometrical mathematical model of the single fin developed in ESATAN-TMS, whereas Figure 4.10 is an example of self-shape array implemented in ESATAN-TMS.
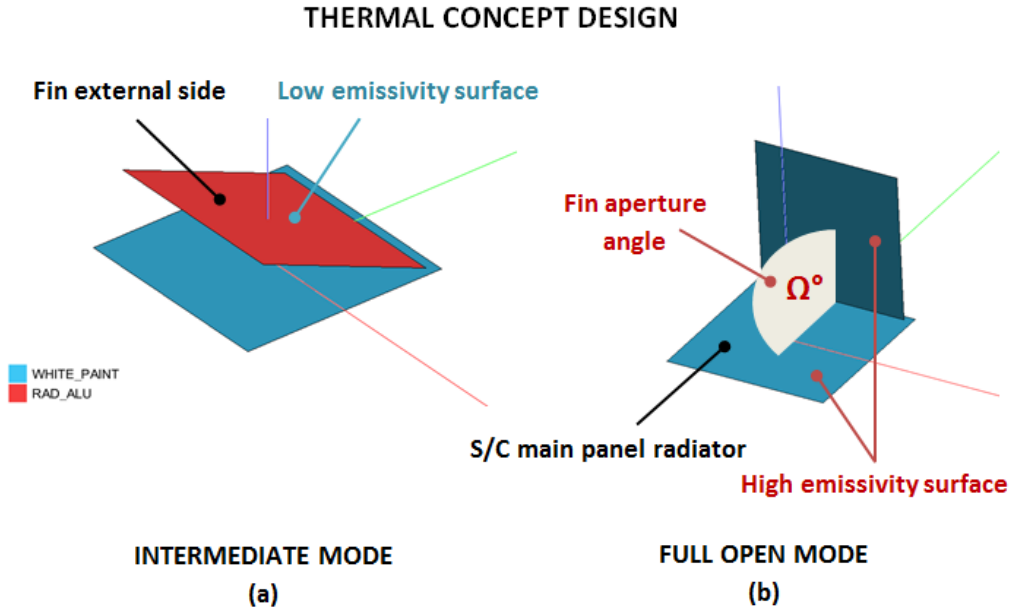
Figure 4.9 Materials combination on the unit cell structure developed in ESATAN-TMS.

41
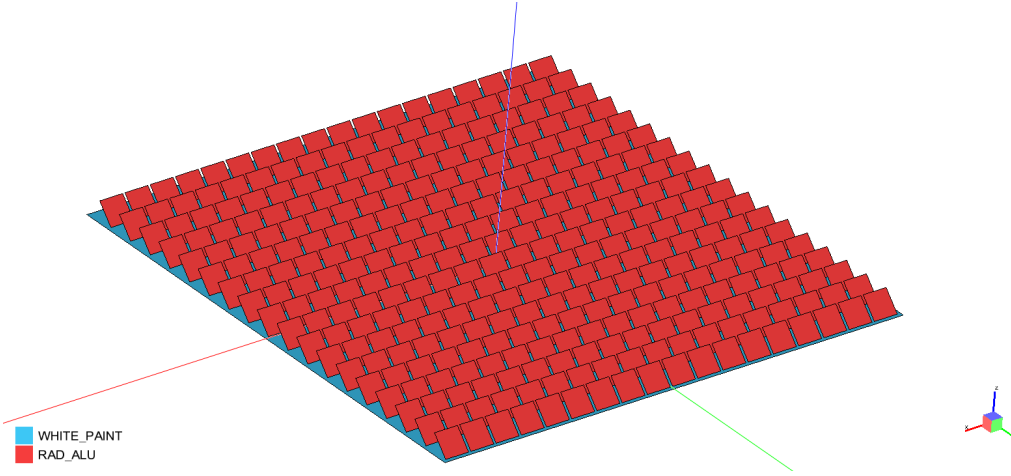
Figure 4.10 Geometrical Mathematical Model of optimized self-shaped array developed in ESATAN-TMS workbench.

The analysis of the three fin's configurations reported in Table 4.2, corresponding to size (H_f) 3 mm, 6 mm, 10 mm, in fully open mode gives the following results (Table 4.3).

Table 4.3 2nd optimization criterion: selected configurations for a 200x200 mm array.

Fin aperture angle [deg]	Fin dimension	GR [W/K^4]		
		3 mm	6 mm	10 mm
0		$6.0 \cdot 10^{-3}$	$2.0 \cdot 10^{-3}$	$4.0 \cdot 10^{-3}$
22.5		$1.0 \cdot 10^{-2}$	$9.0 \cdot 10^{-2}$	$9.0 \cdot 10^{-2}$
45		$1.6 \cdot 10^{-2}$	$1.5 \cdot 10^{-2}$	$1.5 \cdot 10^{-2}$
67.5		$1.9 \cdot 10^{-2}$	$1.8 \cdot 10^{-2}$	$1.9 \cdot 10^{-2}$
90		$2.0 \cdot 10^{-2}$	$2.0 \cdot 10^{-2}$	$2.1 \cdot 10^{-2}$

The case implementing a 10 mm fins size seems to be a good trade-off solution in terms of either GR value (Figure 4.11) and costs (i.e. less number of fins than 6 mm fins configuration).

Even though a minor fin dimension led to higher GR due to a reduced shaping factor on radiator surface, the way fins are arranged highly affects the overall GR of the array. According to equations (4.15) and (4.16), smaller fins means higher view factor but it results also in an increment in the number of responsive structures. As a consequence, the smaller unit cells the more GR to environment decreases due to fins high packing density causing mutually interactions. If we do not rely on the minimization of residual high emissivity area of the radiator, we could observe that decreasing the height of the fins,
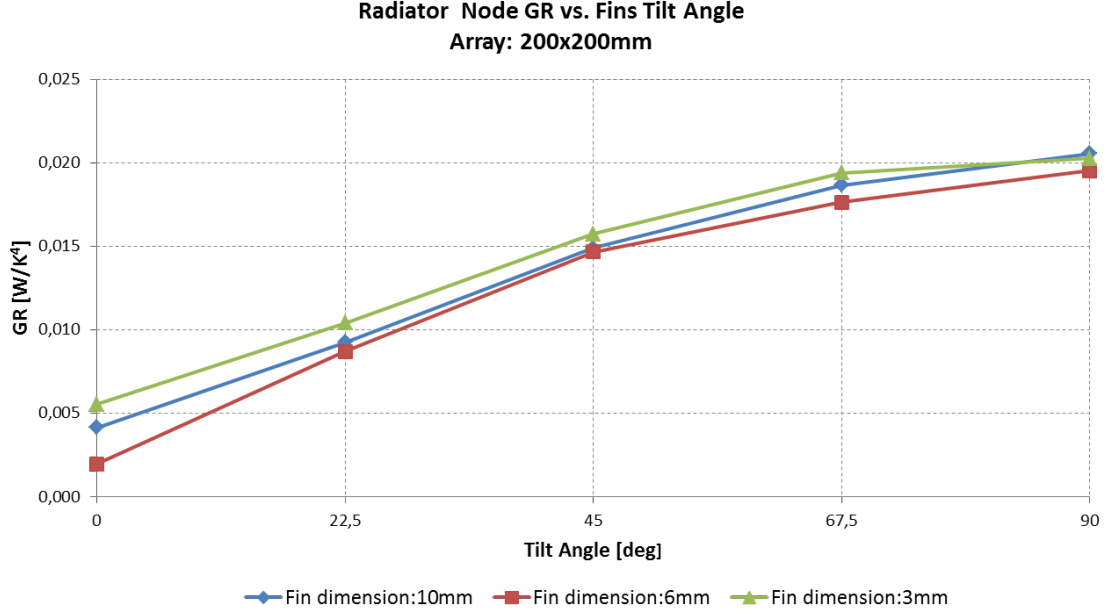
Figure 4.11 Radiative conductor as a function of the tilt angle fo the fin.

while keeping constant the spatial displacements between fins, produces an increment in the view factor of the main radiator panel towards space as we might logically expect. This solution needs to be carefully evaluated through a more in depth thermal study in order to determine how temperatures profile of spacecraft internal units behaves and if actually the present configuration allows to any power savings from heaters. In chapter 5 we will study the set-up implementing fins with $H_\text{f} = 3\,mm$, $w_\text{f} = 10\,mm$) and $\delta_\text{b} = 1.5\,mm$.

It is clear from Figure 4.11 that the spacecraft main panel radiator sees an increasing portion of space as the fins moves from a completely close configuration ($\Omega = 0\,°$) to a fully open one ($\Omega = 90\,°$). This behaviour is related to the shading effect exerted by the fins on the underneath radiator panel, changing its view factor towards space. A modification in the view factor of the main radiator surface is responsible of a subsequent variation of the heat flux rate dissipated by the spacecraft radiator, thus resulting in a reduced emissivity value.

Chapter 5

Thermal Analysis

The next design step consists in simulating the physical behaviour of the smart self-shape radiator for a real space mission.

5.1 Geometrical Mathematical Model definition

Based on the results obtained with the design optimization procedure, a detailed numerical model of the bioinspired radiator installed in a simplified satellite model [20] was developed using ESA standard software for thermal simulation, namely ESATAN-TMS. The model comprises an antenna, three smart radiators and internal units, as shown in Figure 5.1 and Figure 5.2. The spacecraft are covered by MLI in all its external side with the exception of the radiator areas on +/-Y and +X panels where internal units are installed. High power dissipation units (TWT) are mounted on heat pipes, while low power dissipation units are assembled in direct contact with the panels [20]. The thermo-optical properties adopted for the various thermal finishes are summarized in Table 5.1.

Table 5.1   Thermo-optical properties adopted for the satellite surfaces.

Surface	Coating	Emissivity	Absorptivity
Internal panels	black paint	0.85	-
Internal units	black paint	0.85	-
External panels	MLI	0.87	0.94
Radiator surface and lower fins	white paint	0.90	0.15
Radiator upper fins	aluminized paint	0.035	0.15

RADIATOR CELL

UPPER FIN = aluminum
Eps = 0.035

LOWER FIN &
RADIATOR =

white paint - Eps = 0.9

RADIATOR

EASY MODEL – RADIATOR WITH "FULL FINS"
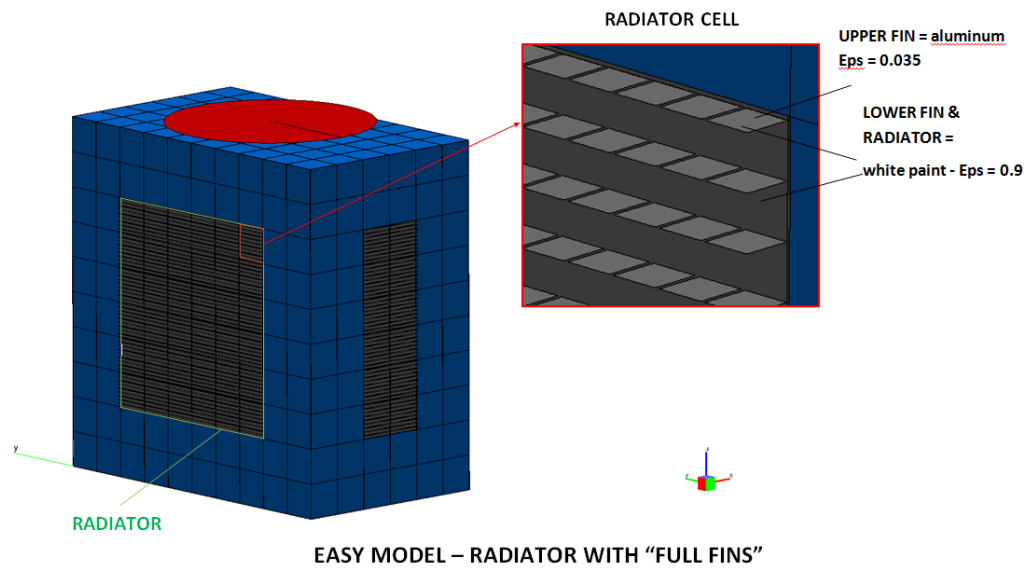
Figure 5.1   Geometrical Mathematical Model of the simply satellite: external side view.

HEATPIPES

BTA

TWT E5

FGUU

TWT E6

TWT E1

OMUX
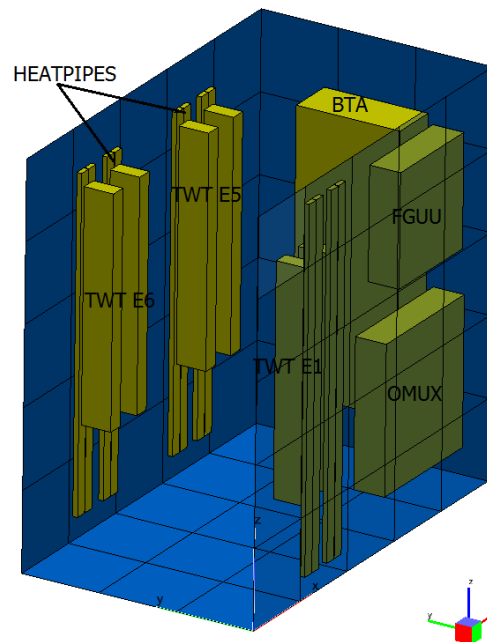
Figure 5.2   Geometrical Mathematical Model of the simply satellite: internal side view.

46

Each radiator is composed by a certain number of arrays, with dimension 200x200mm, according to its radiating area (Figure 5.3). Based on the optimization procedure, the single array of the radiator consists of an overall number of 324 self-shaped structures having dimension 10x10mm separated by 1mm between each other and by 1.5mm from the radiator's borders. The present arrangement allows a 81% low emissivity coverage of the radiator surface, while the remaining 19% of the overall radiating area is characterized by high emissivity. In order to evaluate the effectiveness of the innovative solution compared
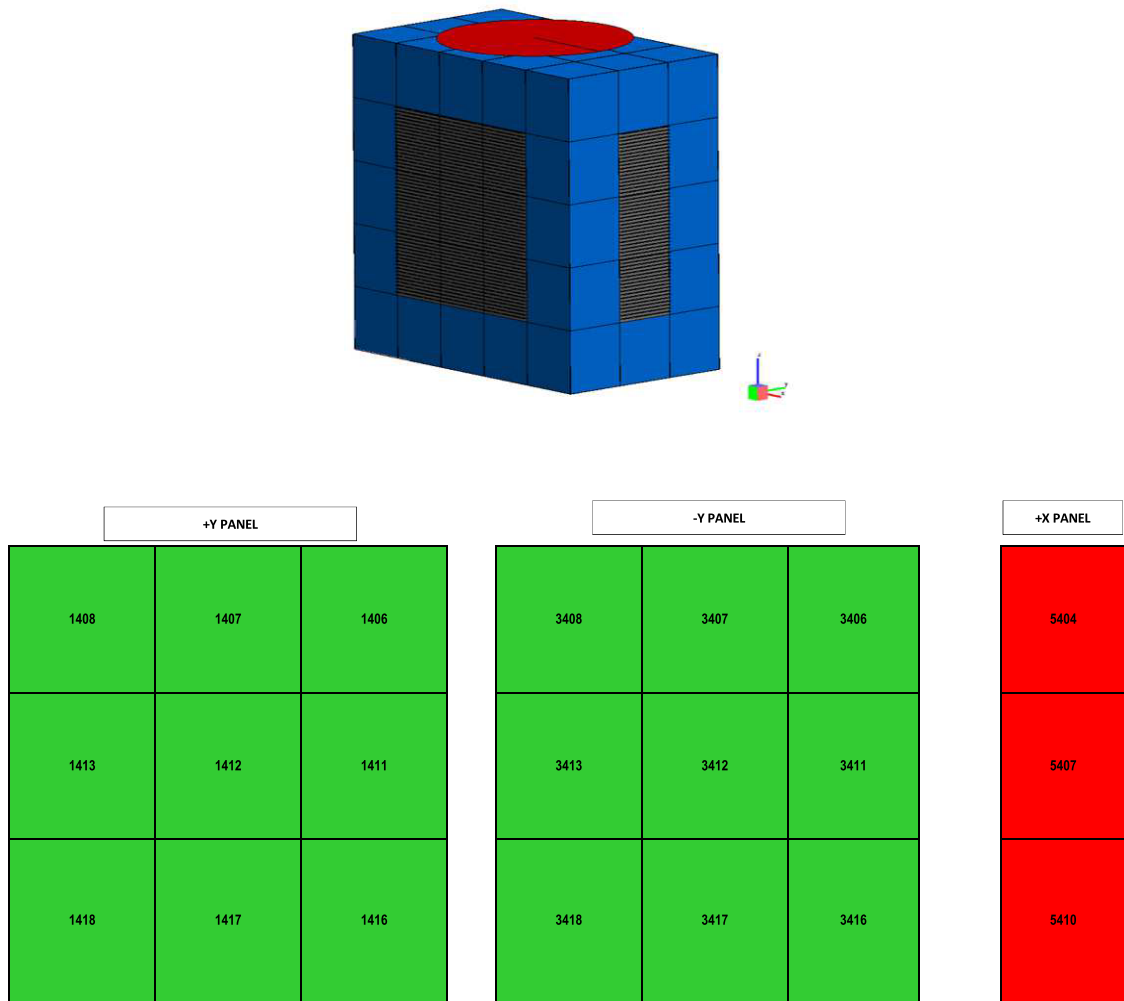
Figure 5.3   Radiator nodes displacements on the +/-Y, +X spacecraft panels.

to the classical one, three different configurations were studied:

- radiator's area totally covered by 10x10mm fins;
- radiator's area totally covered by 3x3mm fins;

47

- radiator's area covered for 50% by 10x10mm fins

Because of the presence of the fins, the GR to space of a single radiator node is reduced respect to the classical flat one. Supposing to fix the spatial distribution of the fins (i.e. $w_f = 1.0\,\text{mm}$; $\delta_b = 1.5\,\text{mm}$) and to modify only the height of the fins, the GR to space decreases from GR = $0.036\,\text{W/K}^4$ of the classical radiator to GR = $0.030\,\text{W/K}^4$ of 3 mm fins and finally to GR = $0.021\,\text{W/K}^4$. Even if the configuration with 3 mm size fins seems to have an higher GR value, its spatial distribution does not fulfil the optimization requirements imposed in chapter 4. The high emissivity area is too wide, nearly 45% of the overall radiator node area, in contrast with the 19% of that of 10 mm fins.
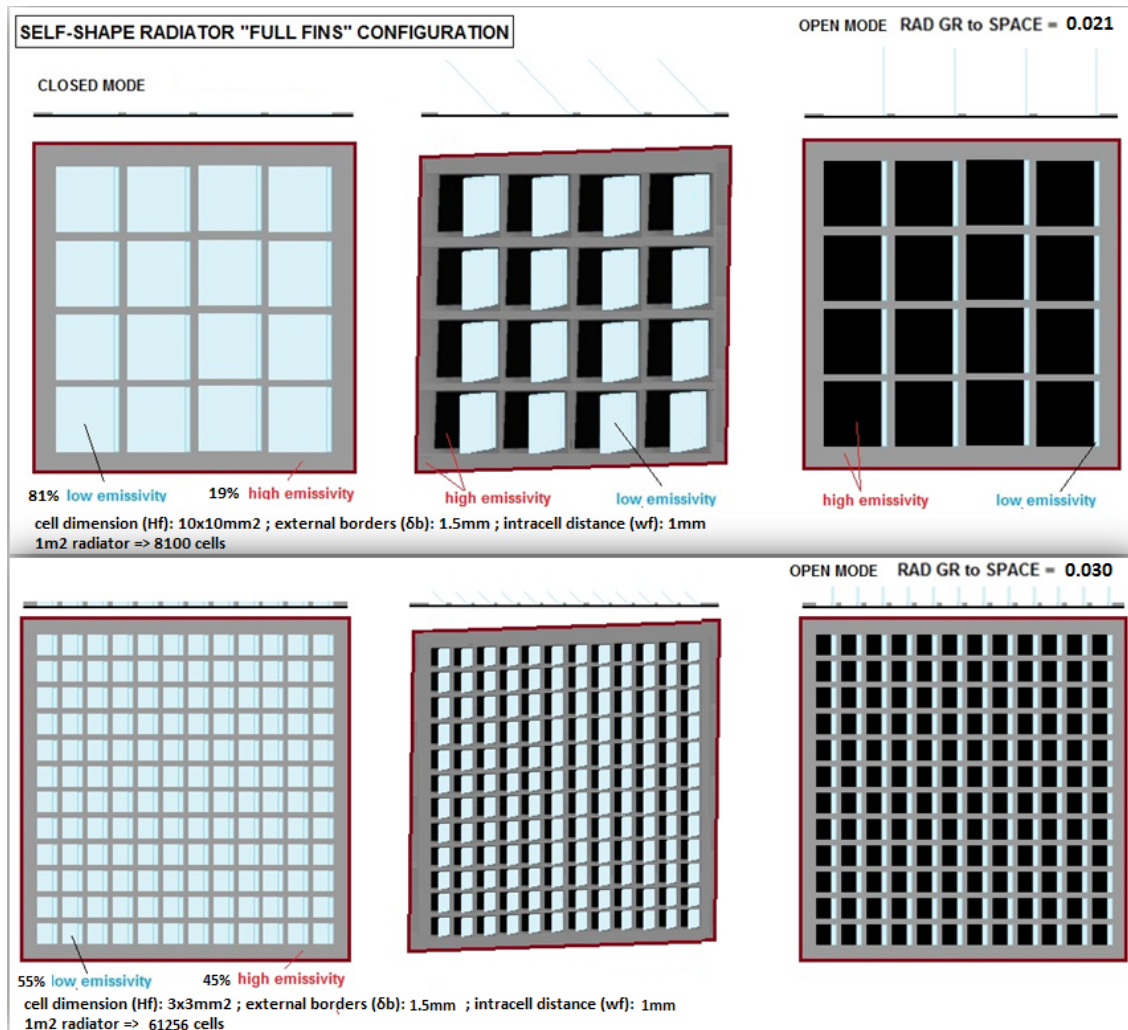
Figure 5.4   Radiator configurations scheme.

48

5.2   Thermal Mathematical Model definition

A preliminary radiative calculation for the overall satellite shows that the radiative conductors (GRs) among the radiator nodes each other's and with the rest of the satellite geometries is of the order of 10^{-5}, and thus negligible (Figure 5.5). This is due to the small dimensions of the fins, which do not exert high shading effects to neighbouring fins that belong to adjacent radiator nodes. This confirms also the effectiveness of the preliminary design optimization process. The distance of the fins to the outer boundary of the radiator node $\delta_b = 1.5$ mm is enough to reduce shading effects between adjacent radiator nodes as well as minimize the high emissivity borders of the array.
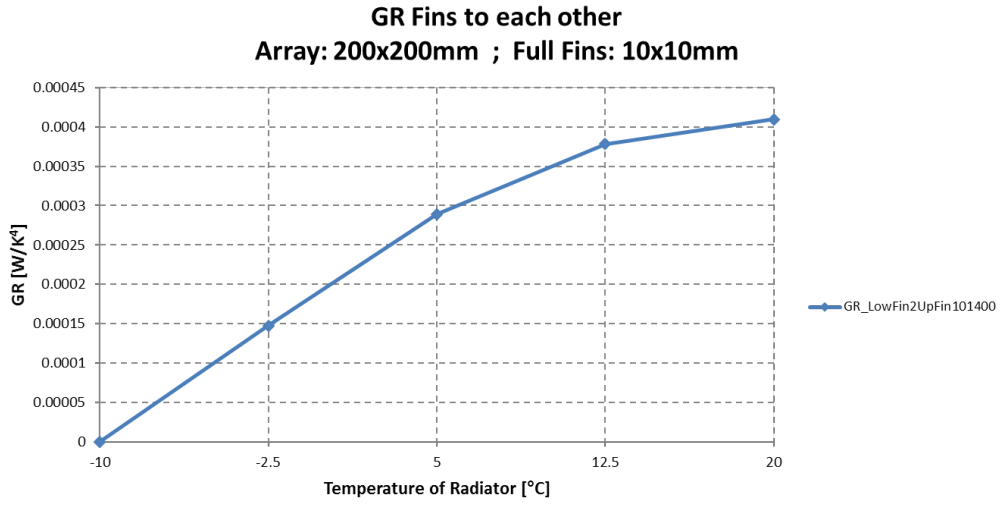
Figure 5.5   GR value of the radiator nodes among each other's.

The present result allows the creation of a one-node radiator model in order to calculate the radiative heat exchanges for each fins' configuration, i.e.:

- radiator surface to upper and lower side of the fins (Figure 5.6);

- radiator surface to space (Figure 5.7);

- upper and lower side of the fins to space (Figure 5.8).

49
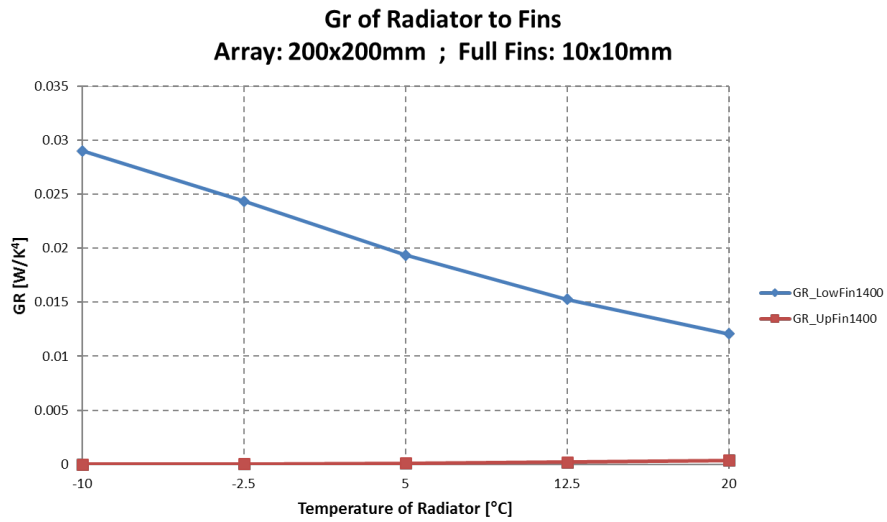
Figure 5.6   GR value of the radiator node relative to upper side (node: 201400) and lower side (node:101400) of the fins.
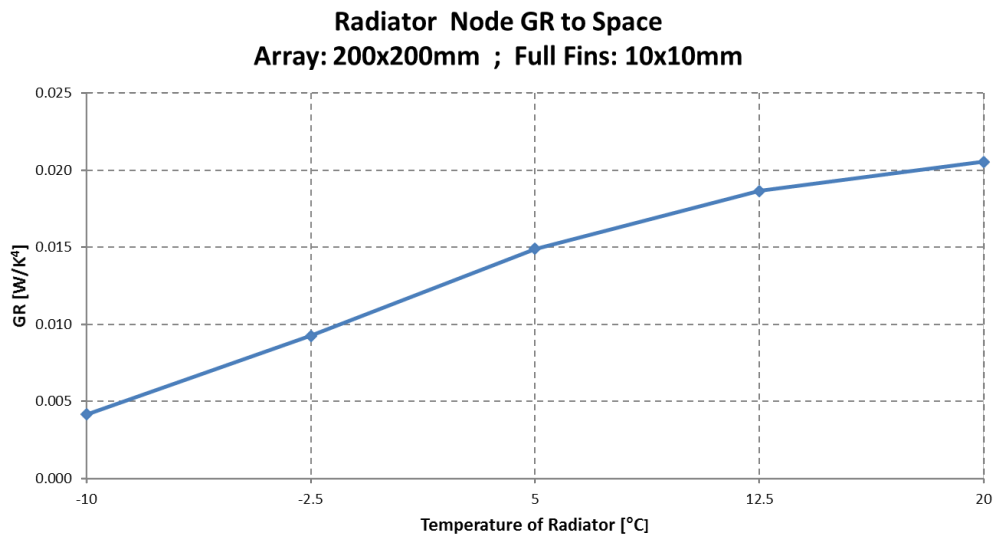
Figure 5.7   GR value of the radiator node towards space.
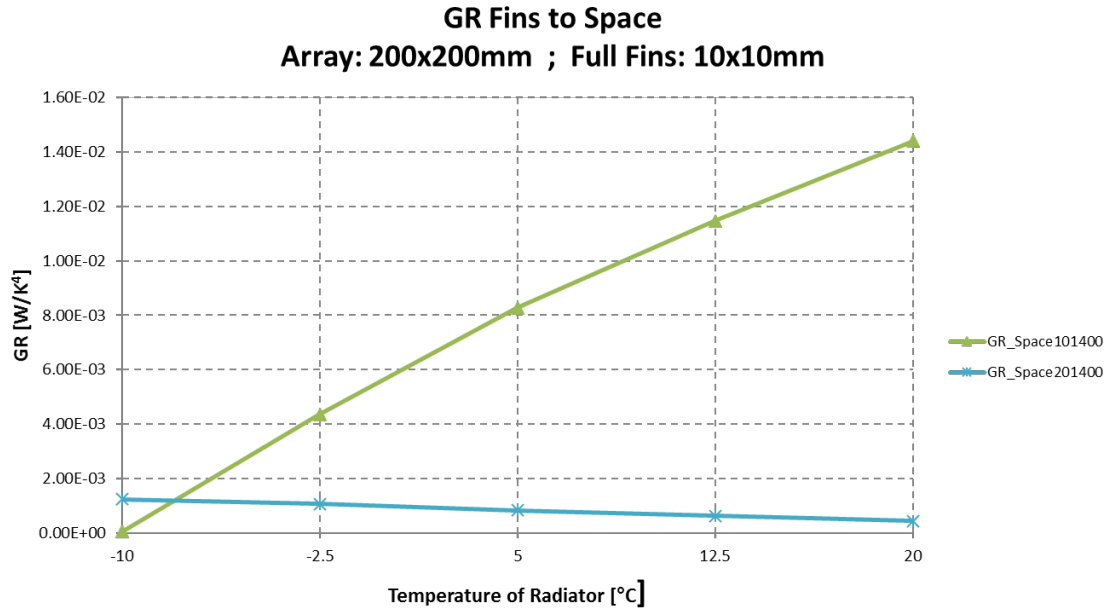
Figure 5.8   GR value of the upper side (node: 201400) and lower side (node:101400) of the fins to space.

Moreover, radiator nodes belonging to the same spacecraft panel (e.g. 14XX, 34XX, 54XX) received nearly the same amount of total external heat power (see Figure5.9). As it can be observed from Figure 5.9, the variation in total heat power absorption is limited to a maximum value inferior to 0.1 W, both in LEO and in MEO. As a result, only one value of the external flux striking the radiator nodes of the same panel shall be calculated for each configuration, thus simplifying the analysis.

LEO ORBIT		NODE	Heat Power (W)
	+Y Panel	1406	2,202
		1407	2,140
		1408	2,163
		1411	2,187
		1412	2,175
		1413	2,116
		1416	2,126
		1417	2,066
		1418	2,135
	-Y Panel	3406	2,162
		3407	2,074
		3408	2,137
		3411	2,140
		3412	2,060
		3413	2,089
		3416	2,057
		3417	2,026
		3418	2,106
	+X Panel	5404	3,470
		5407	3,533
		5410	3,435
MEO ORBIT		NODE	Heat Power (W)
	+Y Panel	1406	0,006
		1407	0,006
		1408	0,008
		1411	0,004
		1412	0,004
		1413	0,008
		1416	0,004
		1417	0,004
		1418	0,003
	-Y Panel	3406	8,903
		3407	8,904
		3408	8,859
		3411	8,928
		3412	8,931
		3413	8,939
		3416	8,860
		3417	8,904
		3418	8,916
	+X Panel	5404	0,163
		5407	0,157
		5410	0,161

Figure 5.9 Total heat power absorbed by each radiator node of panels +/-Y, +X from a typical LEO and MEO environment.

5.3 A computational tool for the creation of temperature dependent heat flux arrays

In order to take in consideration the variable emissivity properties of the radiator, external fluxes (solar Q_S, albedo Q_A, planetary Q_P) are calculated and then implemented in the thermal model as temperature dependent arrays. In order to reduce the work load of the engineer, a dedicated tool is developed in Matlab.
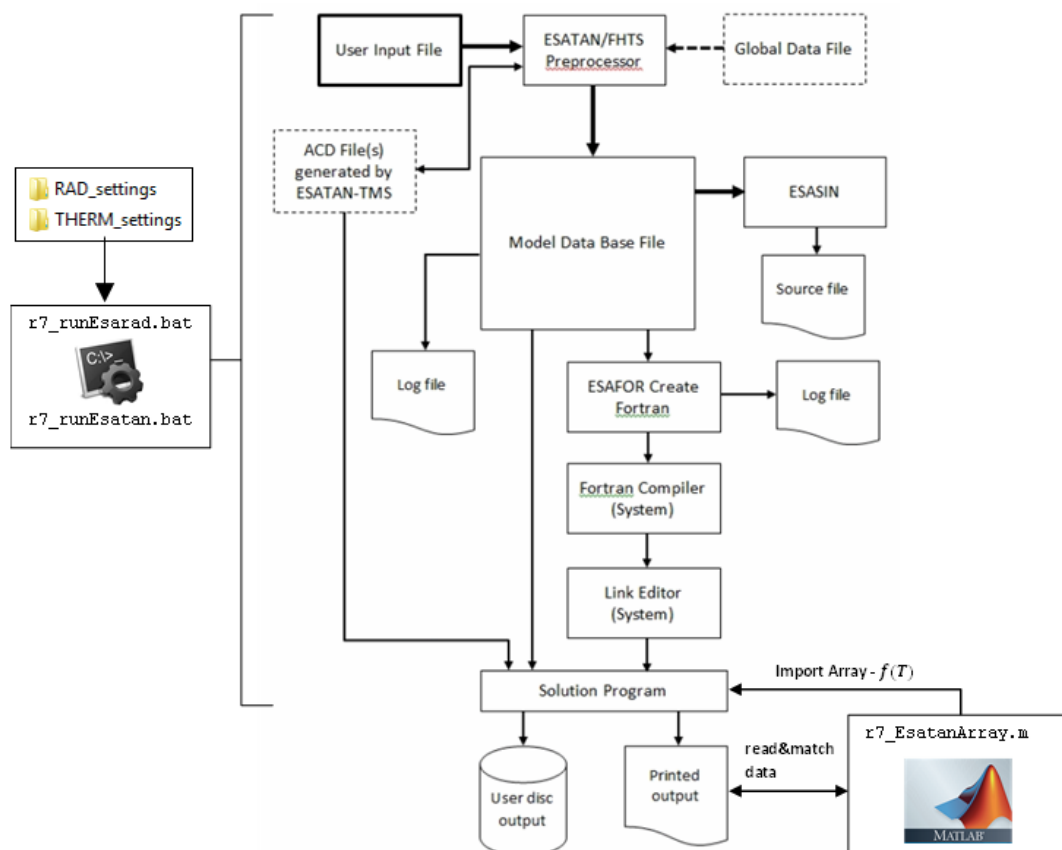
Figure 5.10 The basic ESATAN-TMS flow-chart upgraded with Matlab and DOS codes to improve thermal data management.

The programm coded in Matlab provides an effective thermal data exchanging tool, which allows the user to interface with ESATAN environment. This is achieved by the generation of a text file, which contains temperature dependent arrays of the environmental fluxes acting on the spacecraft surfaces and that can be included in the TMM with the command

$INCLUDE. The algorithm takes advantage of the work performed previously by the program `r7_runEsarad.bat`. This is a DOS `.bat` file of Workbench language statements for the call of ESATAN radiative solver ESARAD in command line mode. The user-defined program allows to launch in the same time multiple radiative cases and to download the correspondent output data, such as environmental heat flux arrays, subroutines for the interpolation of the heat fluxes during orbit, radiative conductors and other informations about the GMM. In order to provide flexibility in the management and creation of the multiple cases to be analysed, input data for `r7_runEsarad.bat` are stored in several files located in the subfolder `RAD_settings`, as reported in table 5.2.

Table 5.2   Files containing the input data read automatically by `r7_runEsarad.bat`.

Input file name	Input data type
`input_modelname.txt`	Name of the model assigned to output and log files
`input_erg.txt`	Geometrical Mathematical Model (GMM) filename
`input_erk.txt`	Radiative filename
`input_ere.txt`	Thermal filename
`input_era.txt`	Administration program filename

Once defined the name of ESATAN output files and the name of the spacecraft thermal nodes on which is detected the heat flux values from the different sources (e.g. solar, albedo, planet), the program `r7_EsatanArray.m` starts to match the thermal flux data needed within the ESATAN output files, in particular in `ARRAYS.data` and `SUBROUTINES.data` files. The values are then manipulated and assembled together in order to finally accomplish the stringent ESATAN format requirements. The process ends with the generation of the output file `EsatanArray.txt`, which can be included in ESATAN TMM file. The figure 5.11 is an example of how the text file will look like.

```
#
QS_1400(TIME, TEMP)
TIME = 0.000000,727.904516,1208.691925,1216.779753,1455.809031,2183.713547,
       2911.618062,3639.522578,4367.427094,5095.331609,5809.922802,5818.010630,5823.236125,
TEMP = -10,0,0,0,0.417866,0.50447,0.568326,0.331685,0,0,0,0,0,0,
TEMP = -2.5,0,0,0,0.29729,0.438527,0.750831,0.634178,0,0,0,0,0,0,
TEMP = 5,0,0,0,0.547496,0.780374,1.2587,1.1329,0,0,0,0,0,0,
TEMP = 12.5,0,0,0,0.806928,1.12641,1.76809,1.80667,0,0,0,0,0,0,
TEMP = 20,0,0,0,1.11702,1.55565,3.10196,2.5735,0,0,0,0,0,0,
```

Figure 5.11   Example of temperature dependent heat fluxes arrays created by `r7EsatanArray.m`.

Finally, the thermal analysis for the different tilt angle configurations of the radiator fins can be launched in command line mode through the executable file `r7_runEsatan.bat`. The present algorithm solves multiple thermal analysis cases, according to the number of model configurations that have been created. The algorithm is trained to collect all the input data by automatically reading from different input files located in the subfolder `THERM_settings`, as summarized in table Table 5.3.

Table 5.3 Files containing the input data read automatically by `r7_runEsatan.bat`.

Input file name	Input data type
`input_TMM_path.txt`	Name of the path where the Thermal Mathematical Model (TMM) is located
`input_TMM_model.txt`	Name of the TMM
`input_TMM_file.txt`	Name of the TMM file

Then, ESATAN is launched and ESAFOR is called in order to generate a FORTRAN 77 file which is then compiled by the system FORTRAN generation process. The result is an executable task that is run on the computer.

```
# Geometrical Mathematical Model (GMM)
filenames
# Insert one filename per row. The total
number of rows represents the overall
cases to be analyzed.
# Comments within the rows must be start
with the symbol '#'.
array_FULLFINS_10mm_0.erg
array_FULLFINS_10mm_22_5.erg
array_FULLFINS_10mm_45.erg
array_FULLFINS_10mm_67_5.erg
array_FULLFINS_10mm_90.erg
```

```
# Thermal Mathematical Model (TMM) filename
# Insert one filename per row. The total
number of rows represents the overall cases
to be analyzed.
# Comments within the rows must be start
with the symbol '#'.
#
EASY10_LEO_CSGLIKE_0.d
EASY10_LEO_CSGLIKE_22_5.d
EASY10_LEO_CSGLIKE_45.d
EASY10_LEO_CSGLIKE_67_5.d
EASY10_LEO_CSGLIKE_90.d
```

(a) **(b)**

Figure 5.12 Example of syntax used to create input data files for `r7_runEsarad.bat` (a) and for `r7_runEsatan.bat` (b).

The tool here presented drastically reduces the time for the setting up of all the source files needed for the execution of the radiative analysis via ESARAD before, and then of the thermal data manipulation in order to account for the heat flux variability with temperature.

5.4 Thermal Analysis results

The thermal analysis of the simply satellite model is conducted for two typical space orbits, namely LEO and MEO, and for both of them either the Cold Case and the Hot Case is evaluated. In particular:

- **LEO** (Cosmo Sky-Med like orbit)

    - **Cold Case:** extreme worst cold environment conditions at beginning of life (BOL), all units switched off except for battery;

    - **Hot Case:** extreme worst hot environment conditions at end of life (EOL), all units switched on;

- **MEO** (Galileo like orbit)

    - **Cold Case:** extreme worst cold environment conditions at beginning of life (BOL), all units switched off except for battery;

    - **Hot Case:** extreme worst hot environment conditions at end of life (EOL), all units switched on;

5.4.1 Results: temperature range of activation $[-10 \div 20]$ °C

Hereafter we present the results derived from the thermal analysis of the simply satellite equipped with smart radiators, the design of which was optimized in chapter 4 for the temperature range of activation $[-10 \div 20]$ °C. It follows the discussion of the results obtained.

- **LEO (Cosmo Sky-Med like orbit)** $\implies$ **Cold Case**

Minimum Non-Operating Temperatures of Interal Units - Worst Cold Case (Survival)

		Not Operating Mode		UFP	CLASSIC		FULL FINS h=10mm f(T): -10°C÷20°C			FULL FINS h=3mm f(T): -10°C÷20°C			HALF FINS h=10mm f(T): -10°C÷20°C		
NODE	Description	Min	Max	±	Tmin predicted	Margin	Tmin predicted	ΔT	Margin	Tmin predicted	ΔT	Margin	Tmin predicted	ΔT	Margin
		[°C]	[°C]	[°C]	[°C]	[°C]	[°C]	[°C]	[°C]	[°C]	[°C]	[°C]	[°C]	[°C]	[°C]
UNITs PANEL +Y															
51151	TWT E5 M	-20	80	10	-17	3	-13	4	7	-14	3	6	-16	1	4
51152	TWT E5 R	-20	80	10	-17	3	-12	4	8	-14	3	6	-16	1	4
51161	TWT E6 M	-20	80	10	-17	3	-15	2	5	-17	0	3	-17	0	3
51162	TWT E6 R	-20	80	10	-17	3	-15	2	5	-17	0	3	-17	0	3
UNITs PANEL -Y															
53111	TWT E1 M	-20	80	10	-17	3	-15	2	5	-17	0	3	-17	0	3
53112	TWT E1 R	-20	80	10	-17	3	-15	2	5	-17	0	3	-17	0	3
53104	FGUU	-40	70	10	-17	23	-11	6	29	-13	4	28	-14	3	26
51111	OMUX	-35	70	10	-19	16	-12	7	23	-14	5	21	-15	4	20
UNITs PANEL +X															
52120	BATTERY	10	40	5	26	16	25	0	15	26	0	16	26	0	16

Figure 5.13   Temperature results for LEO mission application: Cold Case.

Average Power Dissipated by Heaters

LEO Orbit Cold Case		QR	QR	QR	QR
NODE	Description	CLASSIC	FULL FINS h=10mm f(T): -10°C÷20°C	FULL FINS h=3mm f(T): -10°C÷20°C	HALF FINS h=10mm f(T): -10°C÷20°C
UNITs PANEL +Y					
51151	TWT E5 M	7.1	0.0	0.0	0.0
51152	TWT E5 R	7.1	0.0	0.0	0.0
51161	TWT E6 M	15.5	0.0	0.0	7.4
51162	TWT E6 R	15.5	0.0	0.0	0.0
UNITs PANEL -Y					
53111	TWT E1 M	15.3	0.0	0.0	5.4
53112	TWT E1 R	15.3	0.0	0.0	0.0
53104	FGUU	0.0	0.0	0.0	0.0
51111	OMUX	0.0	0.0	0.0	0.0
UNITs PANEL +X					
52120	BATTERY	67.2	57.2	57.2	62.7

Figure 5.14   Power results for LEO mission application: Cold Case.

Heaters Power Budget

LEO Orbit Cold Case	Avg. QR TOT [W]	Peak QR TOT [W]	Avg. ΔW[%]	Peak ΔW[%]
CLASSIC	106	410	-	-
FULL FINS h=10mm	57	130	-46	-68
FULL FINS h=3mm	62	130	-41	-68
HALF FINS h=10mm	75	310	-29	-24

Figure 5.15   Total power results for LEO mission application: Cold Case.

• **LEO (Cosmo Sky-Med like orbit)   ⟹   Hot Case**

Maximum Operating Temperatures of Interal Units - Worst Hot Case

LEO Orbit Hot Case		Operating Mode		UFP	CLASSIC		FULL FINS h=10mm f(T): -10°C÷20°C			FULL FINS h=3mm f(T): -10°C÷20°C			HALF FINS h=10mm f(T): -10°C÷20°C		
NODE	Description	Min	Max	±	Tmax predicted	Margin	Tmax predicted	ΔT	Margin	Tmax predicted	ΔT	Margin	Tmax predicted	ΔT	Margin
		[°C]	[°C]	[°C]	[°C]	[°C]	[°C]	[°C]	[°C]	[°C]	[°C]	[°C]	[°C]	[°C]	[°C]
UNITs PANEL +Y															
51151	TWT E5 M	-10	80	10	48	32	50	2	30	50	3	30	54	6	26
51152	TWT E5 R	-10	80	10	46	34	48	2	32	48	3	32	52	6	29
51161	TWT E6 M	-10	80	10	49	31	51	2	29	51	3	29	55	6	25
51162	TWT E6 R	-10	80	10	46	34	49	2	31	49	3	31	53	6	28
UNITs PANEL -Y															
53111	TWT E1 M	-10	80	10	49	31	51	2	29	52	3	29	55	6	25
53112	TWT E1 R	-10	80	10	47	33	49	2	31	50	3	31	53	6	27
53104	FGUU	-10	50	10	42	8	45	3	5	45	3	5	48	7	2
51111	OMUX	0	50	10	38	12	41	2	9	41	3	9	44	6	6
UNITs PANEL +X															
52120	BATTERY	10	40	5	32	8	36	4	4	36	4	4	39	7	1

Figure 5.16   Temperature results for LEO mission application: Hot Case.

57

Average Power Dissipated by Heaters

LEO Orbit Hot Case		QR	QR	QR	QR
NODE	Description	CLASSIC	FULL FINS h=10mm f(T): -10°C÷20°C	FULL FINS h=3mm f(T): -10°C÷20°C	HALF FINS h=10mm f(T): -10°C÷20°C
UNITs PANEL +Y					
51151	TWT E5 M	0.0	0.0	0.0	0.0
51152	TWT E5 R	0.0	0.0	0.0	0.0
51161	TWT E6 M	0.0	0.0	0.0	0.0
51162	TWT E6 R	0.0	0.0	0.0	0.0
UNITs PANEL -Y					
53111	TWT E1 M	0.0	0.0	0.0	0.0
53112	TWT E1 R	0.0	0.0	0.0	0.0
53104	FGUU	0.0	0.0	0.0	0.0
51111	OMUX	0.3	0.0	0.0	0.0
UNITs PANEL +X					
52120	BATTERY	2.6	2.0	2.4	2.1

Figure 5.17   Power results for LEO mission application: Hot Case.

Heaters Power Budget

LEO Orbit Hot Case	Avg. QR TOT [W]	Peak QR TOT [W]	Avg. ΔW[%]	Peak ΔW[%]
CLASSIC	3	160	-	-
FULL FINS h=10mm	2	160	-21	0
FULL FINS h=3mm	3	160	-9	0
HALF FINS h=10mm	2	160	-19	0

Figure 5.18   Total power results for LEO mission application: Hot Case.

- **MEO (Galileo like orbit) $\implies$ Cold Case**

Minimum Non-Operating Temperatures of Interal Units - Worst Cold Case (Survival)

MEO Orbit Cold Case		Not Operating Mode		UFP	CLASSIC		FULL FINS h=10mm f(T): -10°C÷20°C			FULL FINS h=3mm f(T): -10°C÷20°C			HALF FINS h=10mm f(T): -10°C÷20°C		
NODE	Description	Min	Max	±	Tmin predicted	Margin	Tmin predicted	ΔT	Margin	Tmin predicted	ΔT	Margin	Tmin predicted	ΔT	Margin
		[°C]	[°C]	[°C]	[°C]	[°C]	[°C]	[°C]	[°C]	[°C]	[°C]	[°C]	[°C]	[°C]	[°C]
UNITs PANEL +Y															
51151	TWT E5 M	-20	80	10	-17	3	-14	3	6	-15	2	5	-17	0	3
51152	TWT E5 R	-20	80	10	-17	3	-14	3	6	-15	2	5	-17	0	3
51161	TWT E6 M	-20	80	10	-17	3	-17	1	3	-17	0	3	-17	0	3
51162	TWT E6 R	-20	80	10	-17	3	-17	1	3	-17	0	3	-17	0	3
UNITs PANEL -Y															
53111	TWT E1 M	-20	80	10	-17	3	-15	2	5	-17	0	3	-17	0	3
53112	TWT E1 R	-20	80	10	-17	3	-15	2	5	-17	0	3	-17	0	3
53104	FGUU	-40	70	10	-21	19	-10	11	30	-13	8	27	-16	5	24
51111	OMUX	-35	70	10	-24	11	-12	12	23	-14	10	21	-18	6	17
UNITs PANEL +X															
52120	BATTERY	10	40	5	26	16	26	0	16	26	0	16	26	0	16

Figure 5.19   Thermal analysis results for MEO mission application: Cold Case.

58

Average Power Dissipated by Heaters

MEO Orbit Cold Case		QR	QR	QR	QR
NODE	Description	CLASSIC	FULL FINS h=10mm f(T): -10°C÷20°C	FULL FINS h=3mm f(T): -10°C÷20°C	HALF FINS h=10mm f(T): -10°C÷20°C
UNITs PANEL +Y					
51151	TWT E5 M	24.9	0.0	0.0	4.9
51152	TWT E5 R	24.9	0.0	0.0	0.0
51161	TWT E6 M	34.3	0.0	2.8	13.0
51162	TWT E6 R	34.3	0.0	0.0	0.0
UNITs PANEL -Y					
53111	TWT E1 M	31.8	0.0	1.9	12.4
53112	TWT E1 R	31.8	0.0	0.0	0.0
53104	FGUU	0.0	0.0	0.0	0.0
51111	OMUX	0.0	0.0	0.0	0.0
UNITs PANEL +X					
52120	BATTERY	83.3	67.4	68.3	75.0

Figure 5.20 Power results for MEO mission application: Cold Case.

Heaters Power Budget

MEO Orbit Cold Case	Avg. QR TOT [W]	Peak QR TOT [W]	Avg. ΔW[%]	Peak ΔW[%]
CLASSIC	174	410	-	-
FULL FINS h=10mm	67	130	-61	-68
FULL FINS h=3mm	73	310	-58	-24
HALF FINS h=10mm	105	410	-40	0

Figure 5.21 Total power results for MEO mission application: Cold Case.

- **MEO (Galileo like orbit) $\implies$ Hot Case**

Maximum Operating Temperatures of Interal Units - Worst Hot Case

MEO Orbit Hot Case		Operating Mode		UFP	CLASSIC		FULL FINS h=10mm f(T): -10°C÷20°C			FULL FINS h=3mm f(T): -10°C÷20°C			HALF FINS h=10mm f(T): -10°C÷20°C		
NODE	Description	Min	Max	±	Tmax predicted	Margin	Tmax predicted	ΔT	Margin	Tmax predicted	ΔT	Margin	Tmax predicted	ΔT	Margin
		[°C]	[°C]	[°C]	[°C]	[°C]	[°C]	[°C]	[°C]	[°C]	[°C]	[°C]	[°C]	[°C]	[°C]
UNITs PANEL +Y															
51151	TWT E5 M	-10	80	10	33	47	42	9	38	36	3	44	38	5	42
51152	TWT E5 R	-10	80	10	31	49	40	9	40	34	3	46	36	5	44
51161	TWT E6 M	-10	80	10	33	47	43	10	37	37	4	43	40	6	40
51162	TWT E6 R	-10	80	10	31	49	41	10	39	35	4	45	38	6	43
UNITs PANEL -Y															
53111	TWT E1 M	-10	80	10	34	46	44	10	36	37	3	43	40	5	40
53112	TWT E1 R	-10	80	10	32	48	42	10	38	35	3	45	38	5	42
53104	FGUU	-10	50	10	29	21	38	8	12	30	1	20	33	3	18
51111	OMUX	0	50	10	24	26	34	9	16	26	2	24	28	4	22
UNITs PANEL +X															
52120	BATTERY	10	40	5	26	14	26	1	14	26	0	15	26	0	15

Figure 5.22 Thermal analysis results for MEO mission application: Hot Case.

59

Average Power Dissipated by Heaters

MEO Orbit Hot Case		QR	QR	QR	QR
NODE	Description	CLASSIC	FULL FINS h=10mm f(T): -10°C÷20°C	FULL FINS h=3mm f(T): -10°C÷20°C	HALF FINS h=10mm f(T): -10°C÷20°C
UNITs PANEL +Y					
51151	TWT E5 M	0.0	0.0	0.0	0.0
51152	TWT E5 R	0.0	0.0	0.0	0.0
51161	TWT E6 M	0.0	0.0	0.0	0.0
51162	TWT E6 R	0.0	0.0	0.0	0.0
UNITs PANEL -Y					
53111	TWT E1 M	0.0	0.0	0.0	0.0
53112	TWT E1 R	0.0	0.0	0.0	0.0
53104	FGUU	0.0	0.0	0.0	0.0
51111	OMUX	0.6	0.2	0.5	0.5
UNITs PANEL +X					
52120	BATTERY	32.3	3.2	23.8	16.6

Figure 5.23   Power results for MEO mission application: Hot Case.

Heaters Power Budget

MEO Orbit Hot Case	Avg. QR TOT [W]	Peak QR TOT [W]	Avg. ΔW[%]	Peak ΔW[%]
CLASSIC	33	160	-	-
FULL FINS h=10mm f(T): -10°C÷20°C	4	160	-89	0
FULL FINS h=3mm f(T): -10°C÷20°C	24	160	-26	0
HALF FINS h=10mm f(T): -10°C÷20°C	17	160	-48	0

Figure 5.24   Total power results for MEO mission application: Hot Case.

5.4.2   Discussion of the results: case $[-10 \div 20]$ °C

As it can be seen from figures 5.13 and 5.16, the use of the smart coating provides an overall increment of the temperature values of the spacecraft's internal units in either the Cold Case and the Hot Case with respect to the classical flat radiator. Table 5.4 summarizes the minimum and maximum temperature increment respect to classical solution for the different radiator configuration (i.e. FULL FINS h=10 mm, FULL FINS h=3 mm, HALF FINS h=10 mm).

Compare to classical solution, the half fins configuration shows lower temperature increment than that achieved with a full fins configuration. The full fins with h = 10 mm and h = 3 mm configurations reduces more markedly the thermal gradients between the internal units and provides a more stable temperatures profile. In particular, in Cold Case mode the FULL FINS h=3 mm solution provides quite lower temperature values than FULL FINS

h=10 mm. This is due to the wide high emissivity residual area of the radiator panel (45%) which increases the heat rejected from the satellite and thus lowering the temperature of the internal units. On the other hand, in Hot Case phases an higher value of GR allows to increase the heat flux rejection of the spacecraft towards space environment, avoiding overheating of the electric equipment and providing higher margins from operational temperature limits compare to FULL FINS h=10 mm. If for LEO mission these differences are not markedly distinguishable, for MEO mission the temperature values obtained in Hot Case mode with FULL FINS h=3 mm are $7\,°C ÷ 8\,°C$ lower than FULL FINS h=10 mm configuration.

Table 5.4 Minimum and maximum temperature increments respect to classical solution for the three different radiator configurations: FULL FINS h=10 mm, FULL FINS h=3 mm, HALF FINS h=10 mm.

	LEO (Cosmo Sky-Med like orbit)				**MEO (Galileo like orbit)**			
	Cold Case		**Hot Case**		**Cold Case**		**Hot Case**	
	ΔT_{min}	ΔT_{max}	ΔT_{min}	ΔT_{max}	ΔT_{min}	ΔT_{max}	ΔT_{min}	ΔT_{max}
FULL FINS h=10 mm	2.1	10.3	2.2	3.9	0.5	12.0	0.7	9.9
FULL FINS h=3 mm	0.2	10.3	2.7	3.8	0.1	9.5	1.0	3.6
HALF FINS h=10 mm	0.9	10.3	5.9	7.1	0.1	6.2	3.1	6.3

The increase of temperatures allows heaters to remain inactive and thus avoiding the consumption of electrical power for maintaining the units, except for the battery, within their survivable temperature range. As a result, the average power dissipated by heaters is drastically reduced (Table 5.5).

Table 5.5 Minimum and maximum heaters average power savings for the three different radiator configurations: FULL FINS h=10 mm, FULL FINS h=3 mm, HALF FINS h=10 mm.

	LEO (Cosmo Sky-Med like orbit)		MEO (Galileo like orbit)	
	Cold Case Q[%]	Hot Case Q[%]	Cold Case Q[%]	Hot Case Q[%]
FULL FINS h=10 mm	-46	-26	-61	-90
FULL FINS h=3 mm	-41	-9	-58	-26
HALF FINS h=10 mm	-29	-19	-40	-48

In both Hot and Cold phases, the FULL FINS h = 10 mm configuration achieves the greatest power savings, i.e. up to 61% in Cold Case MEO mode and up to 90% in Hot Case MEO mode.

From temperature and average power results the FULL FINS h = 3 mm configuration seems to be the best solution, allowing limited variation of internal units maximum temperatures in Hot Case mode and low power consumption for thermal management of spacecraft electronic equipment during Cold Case phases. However, problems related to manufacturing feasibility and costs due to the small dimensions and the high number of fins shift the implementation of this choice to the FULL FINS h = 10 mm configuration, at the expense of reduced performance in Hot Case conditions, but still acceptable within the prefixed temperature ranges.

Table 5.6 Best smart radiator configuration selected.

Best Radiator Configuration Selected	
L	200 mm
H_f	10.0 mm
w_f	1.5 mm
δ_b	1.0 mm

5.4.3   Results: temperature range of activation [20 ÷ 25] °C

In order to facilitate the integration activities on earth and to fulfil all the requirements at launch, it is convenient to programmed the behaviour of the self-shape coating within the temperature range [20 ÷ 25] °C. The lower limit is fixed by the thermal requirements inside the faring of the launcher, which are typically set around the room-temperature of 20 °C. Instead, the upper temperature limit is not subjected to particular restrictions, but it must be carefully selected in order to avoid excessive high temperatures during worst hot case environmental conditions that could be affect the integrity of the electronic equipment or of the overall spacecraft itself.

• **LEO (Cosmo Sky-Med like orbit)** ⟹ **Cold Case**

		COLD CASE: COSMO-SkyMed LEO Orbit												
		Operating Mode		Not Operating Mode		UFP	CLASSIC			FULL FINS h=10mm f(T): -10°C÷20°C			FULL FINS h=10mm f(T): 20°C÷25°C		
NODE	Description	Min	Max	Min	Max		QI	Tmin - UFP	QR	Tmin	ΔT	QR	Tmin	ΔT	QR
		[°C]	[°C]	[°C]	[°C]		[W]	[°C]	[W]	[°C]		[W]	[°C]		[W]
	UNITs PANEL +Y														
51151	TWT E5 M	-10	80	-20	80	10	0,0	**-17,0**	7,1	-12,5	4,5	0,0	-4,5	12,6	0,0
51152	TWT E5 R	-10	80	-20	80	10	0,0	**-17,0**	0,0	-12,5	4,5	0,0	-4,4	12,6	0,0
51161	TWT E6 M	-10	80	-20	80	10	0,0	**-17,0**	15,5	-14,9	2,1	0,0	-6,7	10,3	0,0
51162	TWT E6 R	-10	80	-20	80	10	0,0	**-17,0**	0,0	-14,9	2,1	0,0	-6,7	10,4	0,0
	UNITs PANEL -Y														
53111	TWT E1 M	-10	80	-20	80	10	0,0	**-17,0**	15,3	-14,8	2,2	0,0	-5,9	11,1	0,0
53112	TWT E1 R	-10	80	-20	80	10	0,0	**-17,0**	0,0	-14,8	2,2	0,0	-5,9	11,1	0,0
53104	FGUU	-10	50	-40	70	10	0,0	**-16,8**	0,0	-10,9	5,9	0,0	-3,4	13,4	0,0
51111	OMUX	0	50	-35	70	10	0,0	**-19,3**	0,0	-12,2	7,1	0,0	-3,9	15,4	0,0
	UNITs PANEL +X														
52120	BATTERY	10	40	10	40	5	20,0	**25,5**	67,2	25,5	0,0	57,2	25,5	0,0	20

Heater Power Budget					TOT		TOT	ΔW[%]		TOT	ΔW[%]
Average Heater Power [W]					**106**		57	-46		20	-81
Peak Heater Power [W]					**410**		130	-68		130	-68

Figure 5.25   Thermal analysis results for LEO mission application: Cold Case.

• **LEO (Cosmo Sky-Med like orbit)** ⟹ **Hot Case**

		HOT CASE: COSMO-SkyMed LEO Orbit												
		Operating Mode		Not Operating Mode		UFP	CLASSIC			FULL FINS h=10mm f(T): -10°C÷20°C			FULL FINS h=10mm f(T): 20°C÷25°C		
NODE	Description	Min	Max	Min	Max		QI	Tmax	QR	Tmax	ΔT	QR	Tmax	ΔT	QR
		[°C]	[°C]	[°C]	[°C]		[W]	[°C]	[W]	[°C]		[W]	[°C]		[W]
	UNITs PANEL +Y														
51151	TWT E5 M	-10	80	-20	80	10	60,0	**47,7**	0,0	50,1	2,5	0,0	52,7	5,0	0,0
51152	TWT E5 R	-10	80	-20	80	10	0,0	**45,6**	0,0	48,1	2,5	0,0	50,6	5,0	0,0
51161	TWT E6 M	-10	80	-20	80	10	60,0	**48,6**	0,0	51,1	2,5	0,0	53,6	5,0	0,0
51162	TWT E6 R	-10	80	-20	80	10	0,0	**46,5**	0,0	48,9	2,5	0,0	51,5	5,0	0,0
	UNITs PANEL -Y														
53111	TWT E1 M	-10	80	-20	80	10	60,0	**48,9**	0,0	51,2	2,4	0,0	53,8	4,9	0,0
53112	TWT E1 R	-10	80	-20	80	10	0,0	**46,8**	0,0	49,2	2,4	0,0	51,8	4,9	0,0
53104	FGUU	-10	50	-40	70	10	22,0	**41,6**	0,0	44,7	3,1	0,0	47,3	5,7	0,0
51111	OMUX	0	50	-35	70	10	24,2	**38,3**	0,3	40,6	2,2	0,2	43,5	5,2	0,2
	UNITs PANEL +X														
52120	BATTERY	10	40	10	40	5	20,0	**31,9**	2,6	35,8	3,9	2,0	38,2	6,3	1,1

Heater Power Budget					TOT		TOT	ΔW[%]		TOT	ΔW[%]
Average Heater Power [W]					**3**		2	-21		1	-56
Peak Heater Power [W]					**160**		160	0		160	0

Figure 5.26   Thermal analysis results for LEO mission application: Hot Case.

- ## **MEO (Galileo like orbit) $\implies$ Cold Case**

		Operating Mode		Not Operating Mode		UFP	CLASSIC			FULL FINS h=10mm f(T): -10°C÷20°C			FULL FINS h=10mm f(T): 20°C÷25°C		
NODE	Description	Min	Max	Min	Max		QI	Tmin - UFP	QR	Tmin	ΔT	QR	Tmin	ΔT	QR
		[°C]	[°C]	[°C]	[°C]		[W]	[°C]	[W]	[°C]		[W]	[°C]		[W]
	UNITs PANEL +Y														
51151	TWT E5 M	-10	80	-20	80	10	0,0	**-17,1**	24,9	-13,7	3,4	0,0	-8,3	8,8	0,0
51152	TWT E5 R	-10	80	-20	80	10	0,0	**-17,0**	0,0	-13,6	3,4	0,0	-8,3	8,8	0,0
51161	TWT E6 M	-10	80	-20	80	10	0,0	**-17,0**	34,3	-16,5	0,5	0,0	-11,2	5,8	0,0
51162	TWT E6 R	-10	80	-20	80	10	0,0	**-17,0**	0,0	-16,5	0,5	0,0	-11,2	5,8	0,0
	UNITs PANEL -Y														
53111	TWT E1 M	-10	80	-20	80	10	0,0	**-17,1**	31,8	-15,0	2,1	0,0	-9,2	7,9	0,0
53112	TWT E1 R	-10	80	-20	80	10	0,0	**-17,1**	0,0	-15,0	2,1	0,0	-9,2	7,8	0,0
53104	FGUU	-10	50	-40	70	10	0,0	**-21,1**	0,0	-10,5	10,6	0,0	-5,5	15,6	0,0
51111	OMUX	0	50	-35	70	10	0,0	**-23,8**	0,0	-11,8	12,0	0,0	-6,1	17,7	0,0
	UNITs PANEL +X														
52120	BATTERY	10	40	10	40	5	20,0	**25,5**	83,3	25,5	0,0	67,4	25,5	0,0	31,6

Heater Power Budget				TOT		TOT	ΔW[%]		TOT	ΔW[%]
Average Heater Power [W]				174		67	-61		32	-82
Peak Heater Power [W]				410		130	-68		130	-68

Figure 5.27   Thermal analysis results for MEO mission application: Cold Case.

- ## **MEO (Galileo like orbit) $\implies$ Hot Case**

		Operating Mode		Not Operating Mode		UFP	CLASSIC			FULL FINS h=10mm f(T): -10°C÷20°C			FULL FINS h=10mm f(T): 20°C÷25°C		
NODE	Description	Min	Max	Min	Max		QI	Tmax	QR	Tmax	ΔT	QR	Tmax	ΔT	QR
		[°C]	[°C]	[°C]	[°C]		[W]	[°C]	[W]	[°C]		[W]	[°C]		[W]
	UNITs PANEL +Y														
51151	TWT E5 M	-10	80	-20	80	10	60,0	**33,4**	0,0	42,2	8,8	0,0	48,9	15,5	0,0
51152	TWT E5 R	-10	80	-20	80	10	0,0	**31,4**	0,0	40,1	8,7	0,0	46,8	15,5	0,0
51161	TWT E6 M	-10	80	-20	80	10	60,0	**33,3**	0,0	43,2	9,8	0,0	49,7	16,4	0,0
51162	TWT E6 R	-10	80	-20	80	10	0,0	**31,2**	0,0	41,1	9,8	0,0	47,6	16,4	0,0
	UNITs PANEL -Y														
53111	TWT E1 M	-10	80	-20	80	10	60,0	**34,4**	0,0	44,3	9,9	0,0	50,7	16,3	0,0
53112	TWT E1 R	-10	80	-20	80	10	0,0	**32,3**	0,0	42,2	9,9	0,0	48,6	16,3	0,0
53104	FGUU	-10	50	-40	70	10	22,0	**29,4**	0,0	37,9	8,4	0,0	44,8	15,4	0,0
51111	OMUX	0	50	-35	70	10	24,2	**24,4**	0,6	33,7	9,3	0,2	41,3	16,9	0,2
	UNITs PANEL +X														
52120	BATTERY	10	40	10	40	5	20,0	**25,5**	32,3	26,2	0,7	3,5	33,9	8,4	1,3

Heater Power Budget				TOT		TOT	ΔW[%]		TOT	ΔW[%]
Average Heater Power [W]				33		4	-89		1,5	-95
Peak Heater Power [W]				160		160	0		160	0

Figure 5.28   Thermal analysis results for MEO mission application: Hot Case.

In Figure 5.29 are summarized the main differences between the two temperature ranges of activation, namely $[-10 \div 20]\,°C$ and $[20 \div 25]\,°C$, in terms of temperatures and heaters power consumption for a LEO mission scenario. Temperature values are comprehensive of the UFP (Uncertainty Flight Prediction), i.e. $5\,°C$ for the battery and $10\,°C$ for the other components.

Assuming a temperature activation range of $[20 \div 25]\,°C$ for the self-shape radiator allows a further improvement in the average power saving of the heaters up to 81% in Cold Case

and up to 56% in Hot Case. This means an increment of +35% in average power saving compare to the original range of activation of the fins $[-10 \div 20]$ °C, respectively. The reason for this efficiency improvement is mainly related to an overall temperature increase of the internal units, which leads to a further reduction of the electrical power needed to maintain the equipment within its turn-on temperature level. The spacecraft internal units register an average temperature increase of 6 °C, with a peak of +8°C for the FGUU, during the Cold Case phase. Whereas, in Hot Case environmental conditions, the electrical equipment is affected by a lower average temperature growth of about 2.6 °C, with a peak of 2.9 °C for the OMUX. As a result, the power spent by the battery to heat the electronic boxes drastically reduces to 20.1 W in Cold Case and to 1.1 W in Hot Case.

LEO - COSMO Sky-Med like orbit

COLD CASE Results	HOT CASE Results

Temperature budget (Tmin)

CLASSIC	f(T):-10÷20°C	f(T):+20÷25°C	∆Tmin
-17,1	-12,5	-4,5	8,1
-17,0	-12,5	-4,4	8,1
-17,0	-14,9	-6,7	8,2
-17,0	-14,9	-6,7	8,2
-17,0	-14,8	-5,9	8,8
-17,0	-14,8	-5,9	8,8
-16,8	-10,9	-3,4	7,5
-19,4	-12,2	-3,9	8,3
25,5	25,5	25,5	0,0

Temperature budget (Tmax)

CLASSIC	f(T):-10÷20°C	f(T):+20÷25°C	∆Tmax
47,7	50,1	52,7	2,5
45,6	48,1	50,6	2,5
48,6	51,1	53,6	2,6
46,5	48,9	51,5	2,6
48,9	51,2	53,8	2,6
46,8	49,2	51,8	2,6
41,6	44,7	47,3	2,6
38,3	40,6	43,5	2,9
31,9	35,8	38,2	2,4

Power saving

f(T):-10÷20°C	f(T):+20÷25°C	∆Q [%]
-46	-81	35
-68	-68	0

Power saving

f(T):-10÷20°C	f(T):+20÷25°C	∆Q [%]
-21	-56	35
0	0	0

Temperature budget (Tmax)

CLASSIC	f(T):-10÷20°C	f(T):+20÷25°C	∆Tmax
5,1	8,2	17,0	8,8
5,2	8,3	17,1	8,8
5,3	6,1	15,2	9,1
5,3	6,1	15,2	9,1
5,2	6,7	15,6	8,9
5,3	6,7	15,6	8,9
5,0	10,6	18,3	7,7
3,4	9,0	17,3	8,3
25,5	25,5	25,5	0,0
		MaxVal	9,1

Temperature budget (Tmin)

CLASSIC	f(T):-10÷20°C	f(T):+20÷25°C	∆Tmin
17,4	20,5	26,2	5,7
15,4	18,4	24,1	5,7
17,2	20,7	26,8	6,1
15,1	18,6	24,7	6,1
18,7	20,9	26,9	6,0
16,6	18,9	24,9	6,0
9,7	12,4	19,0	6,6
8,4	10,7	18,5	7,8
25,2	25,8	28,2	2,4
		MaxVal	7,8

Figure 5.29 Comparison of thermal analysis results between the two temperature ranges $[\,-10 \div 20\,]$ °C and $[\,20 \div 25\,]$ °C for a LEO typical mission scenario.

In Figure 5.30 are summarized the main differences between the two temperature ranges of activation, namely $[-10 \div 20]$ °C and $[20 \div 25]$ °C, in terms of temperatures and heaters power consumption for a MEO mission scenario. Temperature values are comprehensive of the UFP (Uncertainty Flight Prediction), i.e. 5°C for the battery and 10 °C for the other components.

The use of a temperature activation range of $[20 \div 25]\,°C$ for MEO applications leads to lower thermal efficiency improvements compare to LEO applications. Indeed, heaters save averagely up to 21% more power than $[-10 \div 20]\,°C$ range in Cold Case, while this percentage decreases to 7% in Hot Case. In cold environmental conditions, the FGUU is the unit that is affected by the highest temperature increase (i.e. $+7.8\,°C$) , similar to LEO case. The main differences concerns the Hot Case, where the battery registers reaches $7.7\,°C$. The data of power savings obtained are mainly due to a reduced power consumption from battery operations, i.e. $31.5\,W$ and $1.3\,W$ in Cold and Hot Case, respectively.

MEO - GALILEO like orbit

COLD CASE Results			

Temperature budget (Tmin)

CLASSIC	f(T):-10÷20°C	f(T):+20÷25°C	ΔTmin
-17,1	-13,7	-8,3	5,4
-17,0	-13,6	-8,3	5,4
-17,0	-16,5	-11,2	5,3
-17,0	-16,5	-11,2	5,3
-17,1	-15,0	-9,2	5,8
-17,1	-15,0	-9,2	5,8
-21,1	-10,5	-5,5	4,9
-23,8	-11,8	-6,1	5,7
25,2	25,5	25,5	0,0

Power saving

f(T):-10÷20°C	f(T):+20÷25°C	ΔQ [%]
-61	-82	21
-68	-68	0

Temperature budget (Tmax)

CLASSIC	f(T):-10÷20°C	f(T):+20÷25°C	ΔTmax
10,0	6,6	13,7	7,1
10,0	6,7	13,8	7,1
10,0	4,0	11,1	7,1
10,0	4,0	11,1	7,1
10,0	5,5	13,3	7,8
10,0	5,5	13,3	7,8
10,0	9,9	17,2	7,3
10,0	8,5	16,0	7,5
25,5	25,5	25,5	0,0
		MaxVal	7,8

HOT CASE Results			

Temperature budget (Tmax)

CLASSIC	f(T):-10÷20°C	f(T):+20÷25°C	ΔTmax
33,4	42,2	48,9	6,7
31,4	40,1	46,8	6,7
33,3	43,2	49,7	6,6
31,2	41,1	47,6	6,6
34,4	44,3	50,7	6,4
32,3	42,2	48,6	6,4
29,4	37,9	44,8	6,9
24,4	33,7	41,3	7,6
25,5	26,2	33,9	7,7
		MaxVal	7,7

Power saving

f(T):-10÷20°C	f(T):+20÷25°C	ΔQ [%]
-89	-95	7
0	0	0

Temperature budget (Tmin)

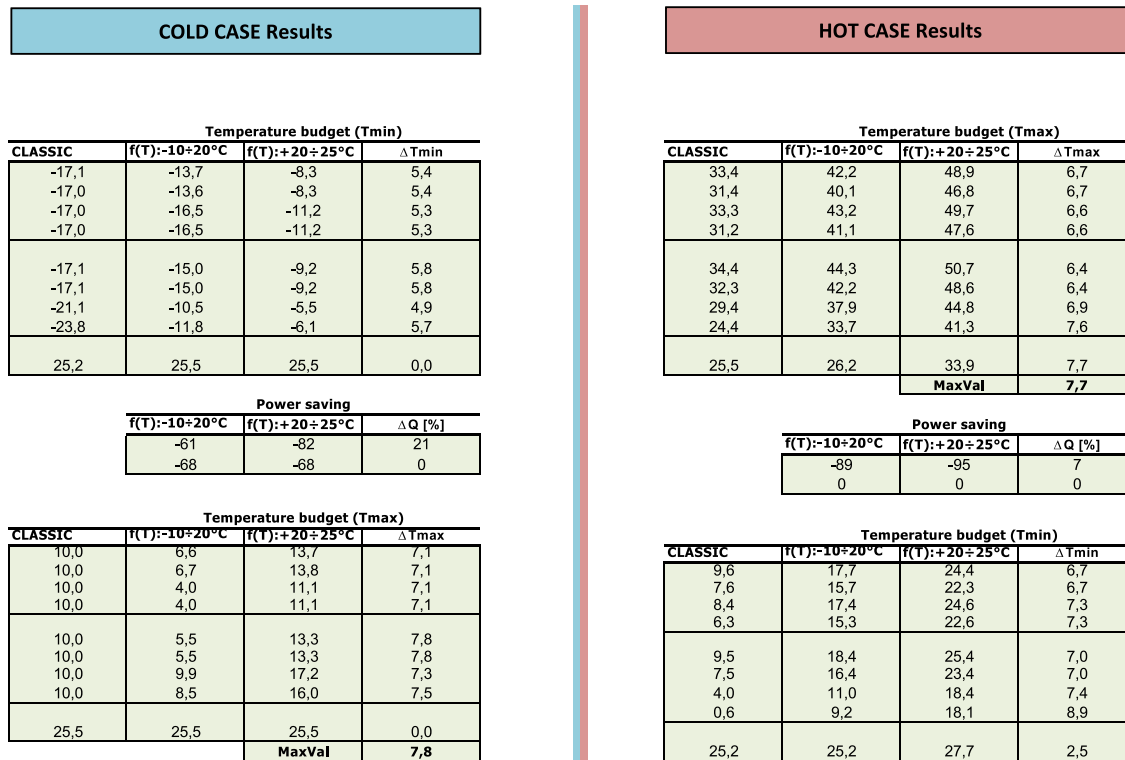| CLASSIC	f(T):-10÷20°C	f(T):+20÷25°C	ΔTmin
9,6	17,7	24,4	6,7
7,6	15,7	22,3	6,7
8,4	17,4	24,6	7,3
6,3	15,3	22,6	7,3
9,5	18,4	25,4	7,0
7,5	16,4	23,4	7,0
4,0	11,0	18,4	7,4
0,6	9,2	18,1	8,9
25,2	25,2	27,7	2,5

Figure 5.30 Comparison of thermal analysis results between the two temperature ranges $[-10 \div 20]\,°C$ and $[20 \div 25]\,°C$ for a MEO typical mission scenario.

5.4.4 Discussion of the results: case $[20 \div 25]\,°C$

In conclusion, the assumption of an higher activation temperature range seems to be beneficial either for the physical integrity and for the optimal performance of the spacecraft internal units. This is in general true in Cold Case phases, where higher units temperature values have a positive impact on the battery operation, reducing the portion of power dedicated to heat the electronic boxes. Moreover, from Figure 5.25 - Figure 5.26 and

Figure 5.27- Figure 5.28 it is clear that the new temperature range provides units with a temperature near the operation limit and far away from critical survivable temperature values. Potential problems could rise in hot conditions due to the delay with which the fins open, limiting the heat exchange of the radiator with space at relatively high temperatures. However, the maximum temperature values reached by the internal units remain well below the operating and non-operating mode upper limits. The most stringent thermal requirements are dictated by the FGUU, the OMUX and battery, which set the upper limit temperature to $50\,°\text{C}$ and to $40\,°\text{C}$, respectively. In both cases, the smart radiator, which is responsive within the range $[20 \div 25]\,°\text{C}$, force the temperature to remain averagely $6\,°\text{C}$ below those thermal specifications.

Chapter 6

Conclusions

The thermal analysis results demonstrate that the use of bioinspired self-shape materials is extremely beneficial for a spacecraft thermal control. The innovative solution provides a significant reduction of heaters power dissipation saving up to 61% in the worst cold case (MEO orbit) respect to a traditional thermal control system. For a typical LEO orbit these numerical results relative to power saving slightly decrease to 46% in the cold case. The effectiveness of the smart radiator is confirmed by the temperature values increment of up to 10°C÷12°C in cold case condition, thus preventing undercooling of spacecraft internal units. On the contrary, the increment on temperatures represents a critical aspect in Hot Case orbital phases, reducing the performance of the radiator compared to classical one solution. This is logically explained by the fact that adding the responsive structures on the radiator panel reduces its view factor to space. With respect to a common OSR plain radiator, having a view factor equal to unity, this reduction is of the order of 42 % (REF = 0.58 W/K^4) for the FULL FINS 10 mm configuration, and of 17 % (REF = 0.83 W/K^4) for the FULL FINS 3 mm solution studied. It is clear that the thermal coating with programmable emissivity must be carefully designed in order to obtain high radiative properties in hot cases, together with low emissivity values in cold cases.

Thermal analysis results described in chapter 5 are hereafter summarized, considering average heater power consumption variation (ΔW) and temperature variation (ΔT) respect to classic radiator. The data are referred to FULL FINS 10 mm and FULL FINS 3 mm configurations.

LEO Orbit (Cosmo SkyMed like) - Cold Case

- Full fins configuration: h = 10 mm

    - Average heater power consumption: ΔW = 46 %
    - Panel +Y (TWTs): ΔT = 2.1 ÷ 4.5 °C
    - Panel -Y (TWTs): ΔT = 2.2 °C

- Panel -Y (FGUU, OMUX): $\Delta T = 5.9 \div 7.1 \, ^\circ C$

- Panel +X (Battery): $\Delta T = 0.0 \, ^\circ C$

- Full fins configuration: h = 3 mm

  - Average heater power consumption: $\Delta W = 41 \, \%$

  - Panel +Y (TWTs): $\Delta T = 0.2 \div 2.9 \, ^\circ C$

  - Panel -Y (TWTs): $\Delta T = 0.3 \, ^\circ C$

  - Panel -Y (FGUU, OMUX): $\Delta T = 4.3 \div 5.4 \, ^\circ C$

  - Panel +X (Battery): $\Delta T = 0.0 \, ^\circ C$

LEO Orbit (Cosmo SkyMed like) - Hot Case

- Full fins configuration: h = 10 mm

  - Average heater power consumption: $\Delta W = 21 \, \%$

  - Panel +Y (TWTs): $\Delta T = 2.5 \, ^\circ C$

  - Panel -Y (TWTs): $\Delta T = 2.4 \, ^\circ C$

  - Panel -Y (FGUU, OMUX): $\Delta T = 3.1 \div 2.2 \, ^\circ C$

  - Panel +X (Battery): $\Delta T = 3.9 \, ^\circ C$

- Full fins configuration: h = 3 mm

  - Average heater power consumption: $\Delta W = 9 \, \%$

  - Panel +Y (TWTs): $\Delta T = 2.7 \div 2.8 \, ^\circ C$

  - Panel -Y (TWTs): $\Delta T = 2.6 \div 2.7 \, ^\circ C$

  - Panel -Y (FGUU, OMUX): $\Delta T = 3.4 \div 2.7 \, ^\circ C$

  - Panel +X (Battery): $\Delta T = 3.8 \, ^\circ C$

MEO Orbit (Galileo like) - Cold Case

- Full fins configuration: h = 10 mm

  - Average heater power consumption: $\Delta W = 61 \, \%$

  - Panel +Y (TWTs): $\Delta T = 0.5 \div 3.4 \, ^\circ C$

  - Panel -Y (TWTs): $\Delta T = 2.1 \, ^\circ C$

  - Panel -Y (FGUU, OMUX): $\Delta T = 10.6 \div 12.0 \, ^\circ C$

  - Panel +X (Battery): $\Delta T = 0.0 \, ^\circ C$

- Full fins configuration: h = 3 mm

    - Average heater power consumption: $\Delta W = 58\%$
    - Panel +Y (TWTs): $\Delta T = 0.0 \div 2.2\,°C$
    - Panel -Y (TWTs): $\Delta T = 0.1\,°C$
    - Panel -Y (FGUU, OMUX): $\Delta T = 7.7 \div 9.5\,°C$
    - Panel +X (Battery): $\Delta T = 0.0\,°C$

MEO Orbit (Galileo like) - Hot Case

- Full fins configuration: h = 10 mm

    - Average heater power consumption: $\Delta W = 89\%$
    - Panel +Y (TWTs): $\Delta T = 8.7 \div 9.8\,°C$
    - Panel -Y (TWTs): $\Delta T = 9.9\,°C$
    - Panel -Y (FGUU, OMUX): $\Delta T = 8.4 \div 9.3\,°C$
    - Panel +X (Battery): $\Delta T = 0.7\,°C$

- Full fins configuration: h = 3 mm

    - Average heater power consumption: $\Delta W = 26\%$
    - Panel +Y (TWTs): $\Delta T = 2.6 \div 3.6\,°C$
    - Panel -Y (TWTs): $\Delta T = 2.6 \div 2.7\,°C$
    - Panel -Y (FGUU, OMUX): $\Delta T = 1.0 \div 1.8\,°C$
    - Panel +X (Battery): $\Delta T = 0.0\,°C$

It is clear from the data summarized above, that the FULL FINS 3 mm configuration is the best solution. Indeed, fins with 3x3 mm dimensions allow to realize an heat radiation capability similar to the classic thermal system in Hot Case, with a modest increment of up to 3.6 °C (MEO orbit) in temperature values of the electronic equipment. On the other hand, in Cold Case temperatures are up to 9.5 °C (MEO orbit) higher than classic radiator, especially for FGUU and OMUX electronic boxes. Moreover, difference between maximum and minimum temperatures is reduced enabling smaller thermal gradients in either operational and non-operational mode. The main advantages are:

- reduction of heater lines and relevant controls (thermistors and computer boards) with consequent decrease of costs;

- to relax the thermo-mechanical constraints;

- to increase the electronic equipment lifetime,

- to increase the performance of radiofrequency systems for telecommunication satellites.

If in Cold Case phase the FULL FINS 3 mm configuration provides approximately the same values of temperature variations and average heater power savings of the FULL FINS 10 mm, in Hot Case mode the former has nearly 7 °C of temperatures difference respect to the latter. However, temperatures with the FULL FINS 10 mm configuration still remains inside the operating and non operating temperature limits. The FULL FINS 3 mm, solution is limited to the actual technological manufacturing level, which requires specific equipment with consequent high manufacturing costs. Therefore, a thermal coating with 10 mm programmable fins could be however considered, while waiting for further new technological improvements.

In conclusion, the use of bioinspired responsive materials seems to be a pathway for the development of low cost and lightweight thermal materials and structures due to their capabilities to passively reacting to temperature, thus enhancing the thermal design flexibility of the engineer. All these advantages could led to great expectations also for a potential applicability in Telecommunications, Exploration and Scientific missions.

Bibliography

[1] N. Athanasopoulos and N. J. Siakavellas. "Programmable thermal emissivity structures based on bioinspired self-shape materials". In: *Scientific Reports* 5.1 (2015). DOI: 10.1038/srep17682.

[2] N. Athanasopoulos and N. J. Siakavellas. "Smart patterned surfaces with programmable thermal emissivity and their design through combinatorial strategies". In: *Scientific Reports* 7.1 (Oct. 2017). DOI: 10.1038/s41598-017-13132-6.

[3] E. Bannon, C. Bower, R. Sheth, R. Stephan, P. Chandrasekhar, and B. Zay. "Electrochromic Radiator Coupon Level Testing and Full Scale Thermal Math Modeling for Use on Altair Lunar Lander". In: International Conference on Environmental Systems (ICES). American Institute of Aeronautics and Astronautics, July 2010. DOI: 10.2514/6.2010-6110. URL: https://doi.org/10.2514/6.2010-6110.

[4] S. Cao, X. Chen, G. Wu, J. Yang, R. Wang, K. Shang, and L. Wang. "Variable Emissivity Surfaces for Micro and Nano-satellites". In: *Physics Procedia* 18 (2011), pp. 91–94. DOI: 10.1016/j.phpro.2011.06.064.

[5] T. J. Cognata, D. Hartl, R. Sheth, and C. Dinsmore. "A Morphing Radiator for High-Turndown Thermal Control of Crewed Space Exploration Vehicles". In: *Proceedings of 23rd AIAA/AHS Adaptive Structures Conference*. Kissimmee, FL, United States, Jan. 2015.

[6] A. G. Darrin, R. Osiander, J. Champion, T. Swanson, D. Douglas, and L. Grob. "Variable emissivity through MEMS technology". In: *ITHERM 2000. The Seventh Intersociety Conference on Thermal and Thermomechanical Phenomena in Electronic Systems (Cat. No.00CH37069)*. Vol. 1. Las Vegas, LV: IEEE, p. 270. DOI: 10.1109/itherm.2000.866834.

[7] T. David G. Gilmore. *Spacecraft Thermal Control Handbook, Volume I: Fundamental Technologies*. 2nd ed. AIAA, Dec. 11, 2002. 836 pp. ISBN: 188498911X. URL: http://www.ebook.de/de/product/4049736/david_g_gilmore_the_aerospace_corporation_d_gilmore_spacecraft_thermal_control_handbook_volume_i_fundamental_technologies.html.

[8] K. Du, Q. Li, J. Ding, Y. Lu, Z. Cheng, and M. Qiu. "Control over emissivity of zero-static-power thermal emitters based on phase changing material GST". In: *Light Science & Applications* (2016).

[9] ECSS-E-ST-10-04C Working Group. *Space Engineering - Space Environment*. ESTEC, P.O. Box 299, 2200 AG Noordwijk, The Netherlands: ESA Requirements and Standards Division, Nov. 15, 2008.

[10] European Space Agency, ESA. *Variable Emissivity Radiator Breadboard*. Tech. rep. June 10, 2016. Chap. Appendix 1 to AO/1-8706/16/NL/KML.

[11] W. Guo, M. Li, and J. Zhou. "Modeling programmable deformation of self-folding all-polymer structures with temperature-sensitive hydrogels". In: *Smart Materials and Structures* 22.11 (Oct. 2013), p. 115028. DOI: 10.1088/0964-1726/22/11/115028.

[12] D. Hartl and D. C. Lagoudas. "Aerospace Applications of Shape Memory Alloys". In: *Proceedings of the Institution of Mechanical Engineers, Part G: Journal of Aerospace Engineering*. Vol. 221 (Special Issue). 2007, pp. 535–552.

[13] P. Laffez, C. Napierala, M. Zaghrioui, V. T. Phuoc, A. Hassini, and M. R. Ammar. "Thermal emittance changes at the charge ordering transition of (Sm0.35Ca0.65)MnO3". In: *Applied Physics Letters* 93.15 (Oct. 2008), p. 151910. DOI: 10.1063/1.2999372.

[14] C. Lee, H.-U. Oh, and T. Kim. "Fabrication and performance analysis of MEMS-based Variable Emissivity Radiator for Space Applications". In: *Journal of Physics: Conference Series* 557 (Nov. 2014), p. 012082. DOI: 10.1088/1742-6596/557/1/012082.

[15] M. J. Li, T. Adachi, C. A. Allen, S. R. Babu, S. Bajikar, M. A. Beamesderfer, R. Bradley, N. P. Costen, K. Denis, A. J. Ewin, D. Franz, L. Hess, R. Hu, K. Jackson, M. D. Jhabvala, D. Kelly, T. King, G. Kletetschka, A. S. Kutyrev, B. A. Lynch, S. E. Meyer, T. Miller, S. H. Moseley, V. Mikula, B. Mott, L. Oh, J. T. Pontius, D. A. Rapchun, C. Ray, S. Schwinger, P. K. Shu, R. Silverberg, W. W. Smith, S. Snodgrass, D. Sohl, L. Sparr, R. Steptoe-Jackson, R. J. Thate, F. Wang, L. Wang, Y. Zheng, and C. Zincke. "Microshutter array system for James Webb Space Telescope". In: *UV/Optical/IR Space Telescopes: Innovative Technologies and Concepts III*. Ed. by H. A. MacEwen and J. B. Breckinridge. Vol. 6687, 668709. SPIE, July 2007. DOI: 10.1117/12.734152.

[16] J. Matovic, A. Vujanic, C. Kment, and K. Reichenberger. "Space flower: the bionic system for satellite thermal regulation". In: *Design and Nature II: Comparing Design in Nature With Science and Engineering (Design and Nature) (Design and Nature, 6)*. Ed. by M. W. Collins and C. A. Brebbia. WIT Press / Computational Mechanics, 2004, pp. 614–621. ISBN: 1-85312-721-3. URL: https://www.amazon.com/Design-Nature-II-Comparing-Engineering/dp/

`1853127213?SubscriptionId=0JYN1NVW651KCA56C102&tag=techkie-20&`
`linkCode=xm2&camp=2025&creative=165953&creativeASIN=1853127213`.

[17]   C. Menon, M. Broschart, and N. Lan. "Biomimetics and robotics for space applications: challenges and emerging technologies". In: *International Conference on Robotics and Automation - Workshop on Biomimetic Robotics*. IEEE, 2007.

[18]   A. J. Millis. "Lattice effects in magneto resistive manganese perovskites". In: *Nature* 392 (Mar. 12, 1998), pp. 147–150.

[19]   A. Paris, K. Anderson, P. Chandrasekhar, B. Zay, and T. Mcqueeney. "Electrochromic Radiators for Microspacecraft Thermal Control". In: *19th Annual AIAA/USU Conference on small Satellites*. Vol. SSC05-VIII-1. Jan. 2005.

[20]   T. Schillaci, E. Bevilacqua, F. Tessarin, and F. Lumaca. *Bioinspired self-shape smart materials for Thermal Control*. Tech. rep. TNO-STCCPI-0013-TASI-C545. CCPI-I Thermal Control Design Unit (TASI), Jan. 30, 2017.

[21]   *Spacecraft Systems Engineering*. Wiley John + Sons, Aug. 12, 2011. 724 pp. ISBN: 047075012X. URL: `http://www.ebook.de/de/product/14751207/` `spacecraft_systems_engineering.html`.

[22]   O. Speck, D. Speck, R. Horn, J. Gantner, and K. P. Sedlbauer. "Biomimetic bioinspired biomorph sustainable? An attempt to classify and clarify biology-derived technical developments". In: *Bioinspiration & Biomimetics* 12.1 (2017), p. 011004. URL: `http://stacks.iop.org/1748-3190/12/i=1/a=011004`.

[23]   A. R. Studart and R. M. Erb. "Bioinspired materials that self-shape through programmed microstructures". In: *Soft Matter* 10.9 (2014), pp. 1284–1294. DOI: `10.` `1039/c3sm51883c`.